Institute of Aircraft Design
Lehrstuhl für Luftfahrtsysteme

Unsteady Aerodynamics Analysis of a High Aspect Ratio Wing by Means of a Loosely Coupled CFD-FEM Model

Bachelor Thesis

Submitted in partial fulfillment of the requirements for the degree B.Sc. Mechanical Engineering at the Department of Mechanical Engineering of the Technical University of Munich.

Supervised by Prof. Dr.-Ing. Mirko Hornung
Carlos Sebastiá Sáez, M.Sc.
Institute of Aircraft Design

Submitted by Jaime Martín Ferres
Student ID: 03770239

Submitted on July 1, 2023

Sequential number LS-XX XX/XX

Abstract

Flutter analysis relies on three main pillars to obtain a prediction for the behaviour of the structure of an aircraft during flight: the determination of its elastic properties, inertial properties and the unsteady aerodynamics analysis. The aeroelastic problem can be assessed combining these three in a process chain. The objective of such a process chain is the certification of aircraft.

This work focuses on the study of the unsteady aerodynamics of a wing for a flutter analysis making use of Computational Fluid Dynamics (CFD). The results of a modal analysis obtained with a Finite Element Method (FEM) model are applied to the domain in the CFD software as an input. This input provides motion to the elements under study by deforming the mesh. In this work the unsteady aerodynamics of the simulation do not modify the elastomechanical response. It is a loosely coupled simulation. FEM and CFD interact with each other in a unidirectional way.

Two independent vibration modes are applied to the wing as an harmonic motion to study their individual effect on the aerodynamics. The first mode is the symmetric wing bending mode of lowest eigenfrequency. The second mode is a symmetric fuselage bending mode. This eigenmode is chosen based on previous flutter analysis results, which showed a coupling with a symmetric wing bending mode of higher eigenfrequency.

The obtention of the aerodynamic coefficients and the total forces acting over the wing is performed for different flight speeds. The unsteady behaviour of the aerodynamic coefficients is analysed. In the case of the lift, it is also compared to the theoretical flutter of the two-dimensional airfoil at the Mean Aerodynamic Chord. Total forces acting over the wing are studied and the obtention of the Generalized Aerodynamic Forces (GAF) matrix is explained. The elements in the GAF can be compared to the ones obtained with other methods such as the Doublet Lattice Method (DLM) to reach a refined flutter analysis.

Keywords: aeroelasticity; flutter; reduced frequency; unsteady aerodynamics; CFD

Acknowledgements

To my supervisor Carlos, who has had time and patience to explain to me whatever, whenever I needed.

To all the friends that have been part of this journey in Aerospace Engineering from the beginning. Especially to Ginés, Lucía, Ignacio and Cris, who have motivated me and pushed me to being a better person.

To the Xtra2 UPV Team, with whom I could feel I was part of something unique. It is not a 'solo haces avioncitos'.

Y por último y más importante a Coco, Emilio y Daniel, que siempre estarán ahí.

Table of Contents

List of Figures

List of Tables

Glossary

Abbreviations

2D	Two dimensions/Two dimensional
3D	Three dimensions/ Three dimensional
AC	Aerodynamic center
AGARD	Advisory Group for Aerospace Research and Development
AoA	Angle of Attack
CAD	Computer Aided Design
CFD	Computational Fluid Dynamics
CV	Control Volume
DLM	Doublet Lattice Method
DNS	Direct Numerical Simulation
EA	Elastic Axis
EAS	Equivalent Air Speed
FEM	Finite Element Method
FV	Finite Volume
GAF	Generalized Aerodynamic Forces
GVT	Ground Vibration Test
ISA	International Standard Atmosphere
LE	Leading Edge
LES	Large-Eddy Simulation
MAC	Mean Aerodynamic Chord
MSL	Mean Sea Level
ProFla	Process Chain Flutter
RANS	Reynolds-averaged Navier-Stokes
S1	Symmetric Wing Bending Oscillation
S3	Symmetric Wing Bending Oscillation of Higher Frequency
SA	Spalart-Allmaras Turbulence Model
SR2	Fuselage Bending Oscillation of Two Static Nodes
TAS	True Air Speed
TE	Trailing Edge
TUM	Technical University of Munich
URANS	Unsteady Reynolds-Averaged Navier-Stokes

Greek Symbols

α	Angle of attack	$[rad]$
β	Phase constant	$[m]$

Δ	Increment, variation	[−]
γ	Specific heat ratio	[−]
μ	Dynamic viscosity	$[Pa \cdot s]$
ν	Kinematic viscosity	$[\frac{m^2}{s}]$
ω	Eigenfrequency of oscillation of the mode	$[\frac{rad}{s}]$
Φ	Matrix of eigenvectors of the system	$[m]$
ϕ	Velocity potential	$[\frac{m^2}{s}]$
Φ_r	Eigenvector of the vibration mode r	$[m]$
ρ	Air density	$[\frac{kg}{m^3}]$
τ	Wall shear stress	$[Pa]$

Indices

∞	Free-stream conditions	[−]
aer	Aerodynamic	[−]
avg	Average	[−]
F	At the flutter boundary	[−]
gen	Modal coordinates	[−]
j	Number of the vibration mode interacting with r	[−]
MAC	Mean Aerodynamic Chord	[−]
max	Maximum value	[−]
n	Cell number	[−]
n	Number of Cartesian coordinate	[−]
n	Total number of cells	[−]
P	Plunging	[−]
r	Number of the vibration mode applied	[−]
T	Torsion	[−]

Latin Symbols

A	Amplitude of the beam model displacement	$[m]$
a	Non-dimensional distance between the AC and the EA	[−]
a	Speed of sound	$[\frac{m}{s}]$
A_c	Aerodynamic damping matrix	$[\frac{Ns}{m}]$
A_k	Aerodynamic stiffness matrix	$[\frac{N}{m}]$
A_r	Amplitude of the vibration mode r	$[m]$
B	Amplitude constant	[−]
C	Damping matrix of the system	$[\frac{Ns}{m}]$
C	Theodorsen function	$[m]$
c	Chord of the wing, Characteristic length	$[m]$

C_D	Drag coefficient of the 3D wing	$[-]$
C_f	Friction coefficient	$[-]$
C_L	Lift coefficient of the 3D wing	$[-]$
C_m	Moment coefficient in the Y coordinate	$[-]$
C_p	Pressure coefficient	$[-]$
$C_{L,0}$	Lift coefficient for a null angle of attack	$[-]$
$C_{L,\alpha}$	Slope of the lift coefficient	$[\frac{1}{rad}]$
D	Drag applied in the aerodynamic center	$[N]$
F	Real part of the Theodorsen Function	$[-]$
f	Vector of aerodynamic loads	$[-]$
f	Frequency of the vibration mode	$[Hz]$
F_f	Friction forces	$[N]$
F_p	Pressure forces	$[N]$
F_p	Total forces	$[N]$
f_{gen}	Generalized forces	$[m]$
G	Imaginary part of the Theodorsen Function	$[-]$
GAF	Generalized Aerodynamic Forces matrix	$[\frac{m^3}{N}]$
K	Stiffness matrix of a system	$[\frac{N}{m}]$
k	Reduced frequency	$[-]$
K_P	Linear stiffness of the 2D flutter model	$[\frac{N}{m}]$
K_T	Torsional stiffness of the 2D flutter model	$[\frac{N}{rad}]$
L	Lift applied in the aerodynamic center	$[N]$
M	Aerodynamic moment applied in the aerodynamic center	$[N \cdot m]$
M	Matrix of inertial properties	$[kg]$
Ma	Mach number	$[-]$
N	Number of vibration modes considered for the study	$[-]$
p	Eigenvalue of the system	$[-]$
p	Pressure	$[Pa]$
q	Vector of displacements in modal coordinates	$[-]$
q_∞	Dynamic pressure	$[Pa]$
q_F	Flutter dynamic pressure	$[Pa]$
R	Specific gas constant	$[\frac{J}{kgK}]$
Re	Reynolds number	$[-]$
S	Area	$[m^2]$
T	Temperature	$[K]$
T	Period of oscillation	$[s]$
t	Time	$[s]$

U	Velocity	$[\frac{m}{s}]$
u	Vector of displacements of the system in Cartesian coordinates	$[m]$
u_1	Plunging mode of the 2D flutter model	$[m]$
u_2	Torsion mode of the 2D flutter model	$[rad]$
u_i	Velocity components	$[\frac{m}{s}]$
X	Longitudinal coordinate of the reference frame	$[-]$
x_i	Spatial coordinate	$[m]$
Y	Lateral coordinate of the reference frame	$[-]$
y	Horizontal distance	$[m]$
$y+$	Non-dimensional wall distance	$[-]$
Z	Vertical coordinate of the reference frame	$[-]$
Z	Complex magnitude of the generalized forces	$[m]$

1 Introduction

This first chapter serves as a description of the environment in which the thesis is developed, from the background of the project in which it is involved, to the main objectives and mission itself.

1.1 Motivation

This thesis is written as a part of the Process Chain Flutter (ProFla) project of the Technical University of Munich (TUM). The objective of the project is the safe certification and efficient development of small aircraft with high aspect ratio wings at an early design stage. The study of the unsteady aerodynamics of this aircraft include extensive ground and flight tests which allow to validate the numerical tools employed to do research on the flutter phenomenon. These numerical tools include computational methods such as the Doublet Lattice Method (DLM) and Computational Fluid Dynamics (CFD).

The need of corrections for the DLM prediction of the unsteady aerodynamics in the control surfaces during flutter (Palacios et al., 2001) is the main drive for this thesis. Through the tool of CFD and staying in the linear aeroelasticity, the Generalized Aerodynamic Forces (GAF) matrix can be obtained. This matrix from a higher fidelity method helps correct the one obtained through a lower fidelity method in order to reduce the iterations needed (Thelen et al., 2020).

Prior to the CFD implementation a Finite Element Method (FEM) model including the eigenmodes and eigenfrequencies of the reference aircraft structure must be obtained. In this case it has been obtained from the work done by Mendl (2022). The relation between FEM and CFD problems in the scope of this thesis is a loosely coupled solution. In this type of solution each of the problems are computed separately, using as input the data provided by the previous calculation. The FEM model is calculated through a modal analysis and validated through Ground Vibration Tests (GVT). Afterwards, it is inserted in the CFD software and no structural properties are computed during the CFD simulations.

1.2 Objectives and Research Questions

The thesis is focused on the unsteady aerodynamics analysis of a high aspect ratio aircraft at the flutter boundary. The main aerodynamic coefficients and the total forces acting over the wing in the unsteady case are the main outcome from the thesis. The objective is to analyse their behaviour over time. A secondary goal is the obtention of the elements of the GAF matrix. It is also sought the creation of a CFD file that can easily be modified and run to

obtain the information explained above as a part of the ProFla's process chain. From these premises the main question can be derived, whose answer is sought through the completion of the thesis.

Main question: How do the aerodynamics of a wing at the flutter boundary evolve with time?

Other sub questions referring to different aspects are also answered in the scope of the thesis.

Sub questions:

- How can the FEM model from a modal analysis be implemented in CFD?
- How can CFD be implemented in a process chain to complement the DLM?
- How can the elements in the GAF matrix be obtained using CFD?
- How effective is flutter theory for the two-dimensional (2D) section applied to a three-dimensional (3D) case?

1.3 Project Organisation

This work is organised so that it has several chapters. An introduction to the topic under study, where the context and purpose of the thesis is explained. A theoretical background where the main concepts related to the thesis are thoroughly detailed. The state of the art, where the current situation in flutter analysis and CFD coupling is presented. The methodology as the steps followed to perform the simulations and obtention of data. The results, where the outcome of the simulations are presented. The summary and outlook, which answers the questions proposed in the objectives of the thesis.

2 Theoretical Background

This section presents a summary of fundamentals on aeroelasticity, aerodynamics and CFD. Concepts such as vibrations, the unsteady aerodynamics of the wing and the different levels of turbulence modelling are introduced and explained in this section.

2.1 Aeroelasticity

Aeroelasticity studies the interactions among three forces: aerodynamic, inertial and elastic. It is divided into two branches depending on the interaction between the original forces. Static aeroelasticity does not take into account inertial forces or unsteady aerodynamic effects. Dynamic aeroelasticity involves the whole spectrum of forces acting on the structure and its variations over time (Collar, 1978).

The Collar's diagram (Collar, 1978) shows the interactions between aerodynamic, elastic and inertial forces. It is depicted in Figure 2.1. In the scope of this thesis only the dynamic aeroelasticity of the wing of the reference aircraft is studied, focusing more thoroughly on the aerodynamics point of view.

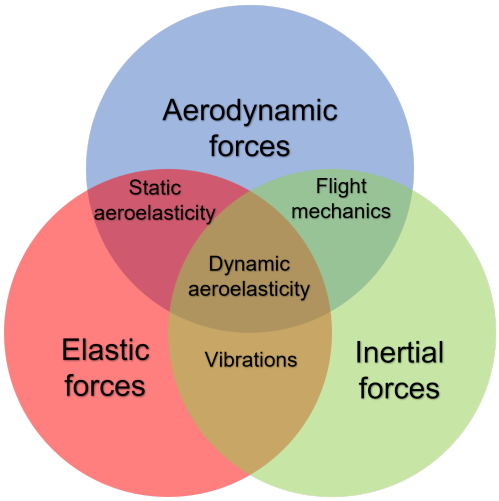

Figure 2.1: Collar's triangle (Collar, 1978)

Different concepts required to assess the dynamic aeroelastic problem are explained. These are the vibration analysis, the generalized forces, the reduced frequency and flutter.

2.1.1 Vibration Analysis

If an object with elastic properties is not subjected to external loads and damping is neglected (Wright and Cooper, 2007), Equation 2.1 describes the movement of the system. In this system inertial and elastic properties are considered constant in time.

$$M\ddot{u}(t) + Ku(t) = 0 \tag{2.1}$$

Where M is the matrix of inertial properties, K is the stiffness matrix and $u(t)$ the time dependent vector of displacements of the system in Cartesian coordinates. The solution to the equation can be assumed of the form $u(t) = \bar{u} \cdot e^{p_r t}$, being $p_r = \pm i\omega_r$. In this case ω_r is the eigenfrequency of each vibration mode of the structure. The eigenvalue problem shown in Equation 2.2 appears after substituting with the solution to the equation (Wright and Cooper, 2007).

$$|K - \omega_r^2 M| = 0 \tag{2.2}$$

As a result the different eigenvectors (Φ_r) of the system are obtained. Each of the eigenvectors and its correspondent eigenfrequency describe one vibration mode. The combination of the different modes considered with their own amplitudes, shapes and frequencies describe the displacements of the system (Wright and Cooper, 2007). The total displacement as a function of the vibrations modes are shown in Equation 2.3.

$$u(t) = \sum_{r=1}^{N} A_r \Phi_r \sin(\omega_r t + \beta_r) \tag{2.3}$$

Where A_r and β_r are the amplitude and initial phase of the N considered vibration modes that depend on the initial conditions proposed for the problem.

In the scope of this thesis the vibration modes of symmetric wing bending oscillation (S1) and the symmetric fuselage bending of two static nodes (SR2) are studied.

2.1.2 Dynamic Aeroelasticity

Dynamic aeroelasticity is studied if the vibration analysis is extended by also considering external aerodynamic forces (Collar, 1978). In the typical airfoil consideration, the modes of plunging (u_1) and torsion (u_2) are studied (Bisplinghoff et al., 1996). They are represented in Figure 2.2.

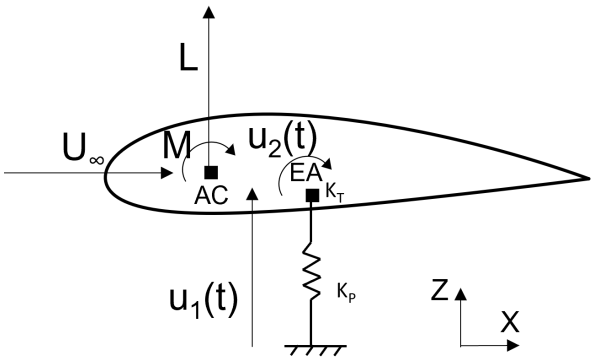

Figure 2.2: 2D coordinates for plunging and torsion

The two stiffnesses are K_P and K_T for plunging and torsion, respectively. In this system the lift (L) and the moment (M) around the aerodynamic center (AC) act as new forces and damping applied to the system. These forces are generated due to the free-stream velocity (U_∞). Drag (D) is neglected (Bisplinghoff et al., 1996) due to its lower order of magnitude compared to lift and its short lever arm to the elastic axis (EA). The system results in the Equation 2.4 (Wright and Cooper, 2007).

$$M\ddot{u}(t) + C\dot{u}(t) + Ku(t) = f(t) \tag{2.4}$$

Where the vector $f(t)$ represents the aerodynamic loads acting over the airfoil and C is the matrix containing the structural damping properties of the system that are now considered.

2.1.3 Obtention of the Generalized Forces

In order to analyse the vibration modes, the translation to modal coordinates can be performed (Wright and Cooper, 2007). The translation from general to modal coordinates is performed through the eigenvectors matrix (Φ) as in Equation 2.5.

$$u(t) = \Phi q(t) \tag{2.5}$$

Where $q(t)$ is the vector of displacements in modal coordinates. For the general case this matrix contains the eigenvectors of each mode in columns ($\Phi = \{\Phi_1, \Phi_2, ..., \Phi_N\}$) (Wright and Cooper, 2007). The two coordinates corresponding to the motion of plunging and torsion are the vibration modes. The 2D case studied is already represented in modal coordinates. The equation of motion is rewritten now in modal coordinates. This is performed through the

translation of the matrices of inertia, damping and stiffness and the vector of loads shown in Equation 2.6.

$$M_{gen} = \Phi^T M \Phi; \quad C_{gen} = \Phi^T C \Phi; \quad K_{gen} = \Phi^T K \Phi; \quad f_{gen} = \Phi^T f \tag{2.6}$$

And the resultant is seen in Equation 2.7.

$$M_{gen}\ddot{q}(t) + C_{gen}\dot{q}(t) + K_{gen}q(t) = f_{gen}(t) \tag{2.7}$$

Which is the time-dependent motion equation in modal coordinates for a system including the aerodynamic loads. This equation is shown reformulated in the frequency domain and normalised to the dynamic pressure (q_∞) (Perry, 2017) in Equation 2.8.

$$(-\omega_r^2 M_{gen} + i\omega_r C_{gen} + K_{gen} - q_\infty GAF(k)) \cdot q_0 = 0 \tag{2.8}$$

Where the $GAF(k)$ matrix is a transfer matrix of complex scalars. These complex scalars (GAF_{rj}) describe the phase and amplitude of the correspondent generalized force ($f_{gen,rj}$). This force acts on the coordinate j due to a harmonic motion of the vibration mode r. Due to being formulated in the frequency domain, the GAF is dependent on the reduced frequency (k).

2.1.4 Reduced Frequency

The reduced frequency is an non-dimensional parameter. It compares the oscillation frequency of the vibration mode with the free-stream velocity and the characteristic length of the problem (Bisplinghoff et al., 1996).

The reduced frequency can also be understood as a comparison between two time measurements: the period of oscillation and the time a fluid particle interacts with the airfoil (Wright and Cooper, 2007). The two time intervals are described in Equations 2.9 and 2.10.

$$T_r = \frac{2\pi}{\omega_r} \tag{2.9}$$

$$T_{aer} = \frac{c}{U_\infty} \tag{2.10}$$

Where T_r is the period of oscillation of the vibration mode r, ω_r is the oscillation frequency in

rad/s, T_{aer} is the time a particle from the leading edge (LE) needs to reach the trailing edge (TE), and c is the chord and characteristic length of the problem. If T_{aer} is divided by T_r one obtains the definition of the reduced frequency as $k = \pi \cdot T_{aer}/T_r$. Its formulation is seen in Equation 2.11.

$$k = \frac{\omega_r c}{2U_\infty} \tag{2.11}$$

A quasi-steady approximation holds for $T_{aer} << T_r$, in which the fluid travels with a relatively high velocity and a displacement of the wing is not perceived by the fluid particles. In a case in which both periods have the same order of magnitude, no effect can be neglected. In those cases, a study of the unsteady aerodynamics must be performed.

2.1.5 Flutter

Flutter can be described in the time domain. Assuming L and M to be linearly dependent on the vibration modes and their derivatives, the motion equation results in Equation 2.12.

$$(M_{gen} + M_{aer})\ddot{q}(t) + (C_{gen} + C_{aer})\dot{q}(t) + (K_{gen} + K_{aer})q(t) = 0 \tag{2.12}$$

Where the matrices M_{aer},C_{aer} and K_{aer} include the coefficients that describe the linear dependence of L and M on $q(t)$.

The solution is once again in the form of $q(t) = \bar{q} \cdot e^{p_r t}$. In this case the real part of p_r is not necessarily equal to 0. Whether the solution has a positive or negative real part can be computed for simple systems (Bisplinghoff et al., 1996) as a function of q_∞. A qualitative evolution of p_r is shown in Figure 2.3.

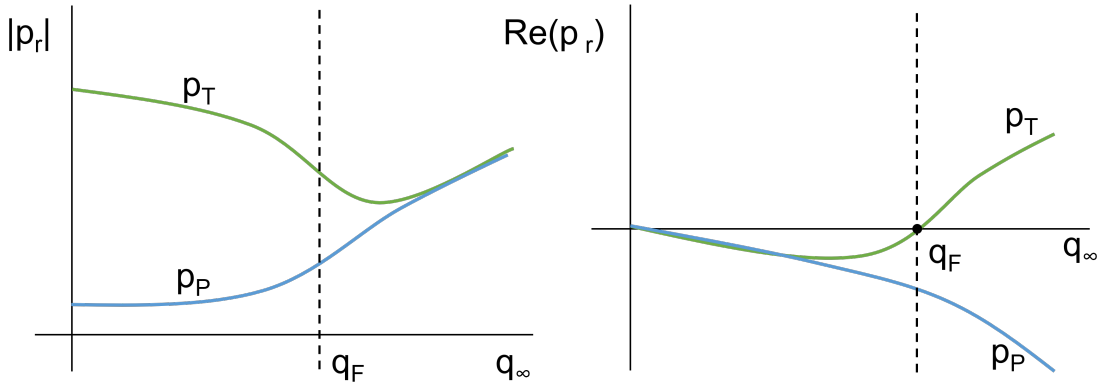

Figure 2.3: Qualitative evolution of the frequency and damping of the 2D case with q_∞

Where the eigenvalues of the torsional (p_T) and plunging (p_P) modes are represented as a function of q_∞.

The dynamic pressure at which the real part of p_r becomes greater than 0 is called the flutter dynamic pressure (q_F). The real part represents the damping of that specific mode. A negative damping is reached when the real part of the eigenvalue becomes positive. This negative damping produces an increase in the amplitude of the oscillation. The absolute value of the eigenvalue represents the frequency of oscillation.

Flutter is the phenomenon that involves the pure harmonic oscillation of one of the modes due to zero damping. A further increase in the real part of the eigenvalue leads to dynamic instability. The mode that becomes unstable is usually the torsional (Bisplinghoff et al., 1996), as depicted in Figure 2.3. The frequencies of each mode modify their value until a mode coalescence takes place. The frequencies of the modes involved reach approximately the same value, and resonate with each other, as seen in the left plot of Figure 2.3.

2.2 Aerodynamics

The aeroelastic problem is assessed from the aerodynamics point of view. The concepts related specifically to unsteady aerodynamics are detailed in this section. These are concepts such as the Theodorsen function and its effect on the aerodynamic coefficients, the total forces acting over the wing or adimensional parameters used for justifying assumptions done in the thesis. The DLM and the assumptions done in the prediction of unsteady aerodynamics are also briefly explained.

2.2.1 Unsteady Lift

The well know equation for the lift generated by a body when presented to fluid conditions and no stall can be seen in Equation 2.13.

$$L = q_\infty S \cdot (C_{L\alpha}\alpha + C_{L,0}) \tag{2.13}$$

In this equation the element of the angle of attack can be divided into an average and a variation ($\alpha = \alpha_{avg} + \Delta\alpha$) when the vibration of the wing is considered. The expression for the lift can be now derived as seen in Equation 2.14.

$$L = L_{avg} + \Delta L = q_\infty S \cdot C_{Lavg} + q_\infty S \cdot C_{L\alpha}\Delta\alpha \tag{2.14}$$

If this equation is brought to the 2D and only $\Delta\alpha$ is considered, the increment in lift per unit span (L') from the well known flutter 2D problem is obtained. It can be seen in Equation 2.15 .

$$\Delta L' = q_\infty c C_{L\alpha} \Delta\alpha \tag{2.15}$$

The variations in the angle of attack for the 2D airfoil can be considered a function of the two plunging and torsion and the reduced frequency such that $\Delta\alpha = f(u_1, \dot{u_1}, \ddot{u_1}, u_2, \dot{u_2}, \ddot{u_2}, k)$. This model is described by Theodorsen (1949) and the non-dimensionalised expression for the lift can be obtained (Brunton and Rowley, 2009). The dimensionalised expression inserted in the increment of lift per unit span is seen in Equation 2.16.

$$\Delta L' = q_\infty C_{L\alpha} c \cdot ((\frac{c\ddot{u_1}}{4U_\infty^2} + \frac{c\dot{u_2}}{4U_\infty} + \frac{c^2 a\ddot{u_2}}{8U_\infty^2}) + C(k) \cdot (\frac{\dot{u_1}}{U_\infty} + u_2 + (\frac{c}{4} + \frac{ca}{2}) \cdot \frac{\dot{u_2}}{U_\infty})) \tag{2.16}$$

Where $C(k)$ is the Theodorsen function (Theodorsen, 1949) and a is the non-dimensional distance between the AC and the EA. This geometric relation can be observed in Figure 2.4.

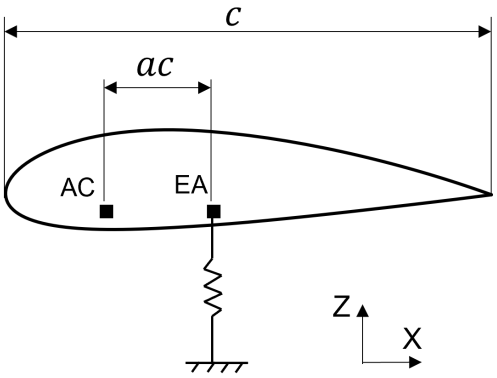

Figure 2.4: Geometrical relation between the aerodynamic center and the elastic axis

The Theodorsen function is dependent on the reduced frequency to determine part of the unsteady behaviour of an oscillating airfoil (Theodorsen, 1949). This function provides a complex number. This complex number modifies the aerodynamic response to the motion taking place in the wing. The variations that it causes are in phase and amplitude. The expression can be seen in Equation 2.17.

$$C(k) = F(k) - iG(k) \tag{2.17}$$

A qualitative plot of the Theodorsen function terms is seen in Figure 2.5.

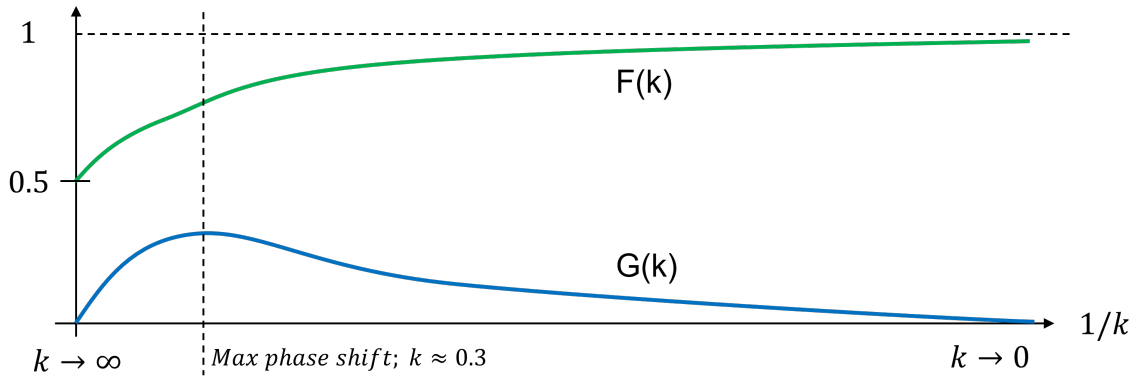

Figure 2.5: Qualitative evolution of the Theodorsen (1949) function

A positive value of both terms $F(k)$ and $G(k)$ implies a negative phase in the complex number. The Theodorsen function delays the response of the aerodynamics of the aircraft with respect to the motion of the wing. This delay disappears for small reduced frequencies, which describes a quasi-steady behaviour of the aerodynamics at $F(k) = 1$ and $G(k) = 0$. The maximum phase shift is produced at $k = 0.3$. This phase shift is approximately of 15°. The module of the Theodorsen function varies, starting at 1 for low k and being 0.5 for very high k-values.

2.2.2 Forces Acting on the Body Surface

The total forces acting on the surface of the body exposed to a fluid flow can be divided into pressure forces and friction forces (Anderson, 2017). The two are described in the following paragraphs.

Pressure Forces

Pressure forces act perpendicularly to the surface of the body. In aerodynamics the parameter used to describe the relative pressure with respect to the free flow is called the pressure coefficient. This non-dimensional number is defined in Equation 2.18.

$$C_p = \frac{p - p_\infty}{q_\infty} \tag{2.18}$$

Where p is the local pressure at the point of the wall that is intended to be studied. The

pressure coefficient is a non-dimensional parameter, as it is a normalisation to the dynamic pressure. When the pressure coefficient is integrated over the whole surface of the body surrounded by the flow, the force normalized to the dynamic pressure F'_p is obtained.

Friction Forces

Friction forces act tangentially to the surface of the body. They are derived from the wall shear forces that appear due to viscosity. The friction coefficient is the adimensional parameter used to take into account this effect. It can be computed as shown in Equation 2.19

$$C_f = \frac{\mu \cdot \frac{dU}{dy}}{q_\infty} = \frac{\tau}{q_\infty} \tag{2.19}$$

Where μ is the dynamic viscosity of the fluid, du/dy is the velocity gradient in the perpendicular direction to the wall and τ is the wall shear stress. When the friction coefficient is integrated over the whole surface of the body, the friction force normalized to the dynamic pressure F'_f is obtained.

2.2.3 Adimensional Free Flow Parameters

Non-dimensional parameters are usually used to characterise certain properties of the fluid. In this case, the Mach number and the Reynolds number are used to assess compressibility and turbulence of the fluid, respectively.

Mach Number

The Mach number is a dimensionless quantity representing the ratio of the flow velocity to the local speed of sound. The Mach number and the speed of sound are described in Equations 2.20 and 2.21.

$$Ma = \frac{U_\infty}{a} \tag{2.20}$$

$$a = \sqrt{\gamma R T} \tag{2.21}$$

Where Ma is the Mach number, a is the speed of sound, γ is the specific heat ratio for the fluid, R is the specific gas constant and T the temperature of the fluid.

Depending on the value of the Mach number different regimes of the fluid are expected (Anderson, 2017). The different behaviours are seen in Figure 2.6.

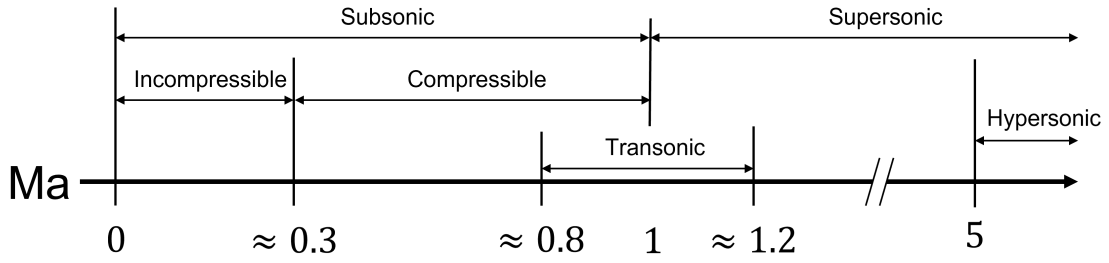

Figure 2.6: Flow regimes over the mach number (Anderson, 2017)

In the scope of this thesis all the simulations cases correspond to a $Ma < 0.3$. This means that the assumption of incompressible flow is justified. Due to this consideration the density is considered constant in every section of the fluid domain.

Reynolds Number

The Reynolds number is a dimensionless quantity that relates inertial to viscous effects and is used to determine if the fluid is turbulent or laminar. It is defined as in Equation 2.22.

$$Re = \frac{U_\infty \rho l}{\mu} = \frac{U_\infty c}{\nu} \tag{2.22}$$

Where Re is the Reynolds number, ρ is the density of the fluid, c is the characteristic length of the problem and μ is the dynamic viscosity. The second definition is with ν, the kinematic viscosity. It is defined as $\nu = \mu/\rho$.

For $Re < 10^6$ part of the fluid is still in a laminar regime, the viscosity effects are still important. For $Re > 10^6$ the fluid can be assumed to be fully turbulent and viscosity effects are considered of minor influence compared to inertial. The main parameter that allows a visualisation of the transition from a laminar to a turbulent flow is the skin friction coefficient. The variation of the skin friction coefficient with the Re over a flat plate is described by Anderson (2017) and is seen in Figure 2.7.

Skin friction coefficient follows two different trends for the two regimes. Transition can be observed over a wide range of Re. Over a certain Re a fully turbulent flow can be assumed if a transition from laminar to turbulent is not the objective of study. In such a study the precise modelling of the boundary layer would be crucial to determine the flow regime over a wall.

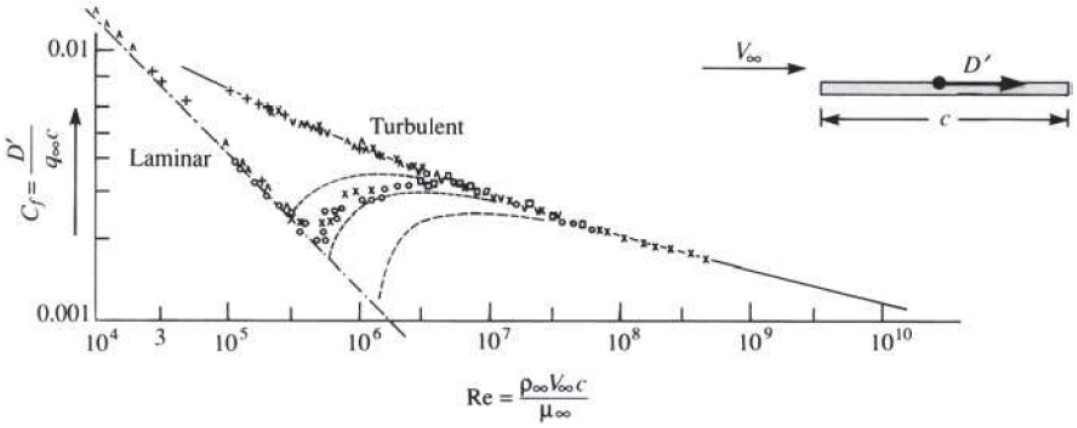

Figure 2.7: Variation of laminar and turbulent skin friction coefficient for a flat plate as a function of Re (Anderson, 2017)

2.2.4 Doublet Lattice Method

In order to solve the unsteady aerodynamics of aircraft, a potential method based on the approximation of the wing to panels in 2D has been used for decades (Albano and Rodden, 1969). The Doublet Lattice Method is used for the flutter analysis in subsonic regime (Albano & Rodden 1968). Potential doublets are set at 1/4-th of the chord of each box that form the panels at the wing (Albano & Rodden 1968). These doublets generate an acceleration of the flow over and under the wing creating the pressure distribution that generates lift (Albano & Rodden 1968). This method for solving the aerodynamics of the wing delivers the GAF matrix previously defined in Section 2.1.2, but does not take into account viscous effects over the wing or considers the thickness of the body.

2.3 Computational Fluid Dynamics

Once the aeroelastic problem has been described, a tool used to manage it is the CFD. The fraction of the field of CFD that is involved in this thesis is briefly described in this section.

Fluid flows and related phenomena can be described by partial differential equations that cannot be solved analytically for the general case, known as the Navier Stokes equations (Versteeg and Malalasekera, 2007). Different discretization methods that approximate the differential equations to algebraic equations can be used to later be solved in computers (Ferzinger and Peric, 2002). The main purpose of CFD is the obtention of detailed solutions to the Navier-Stokes equations that serve as an alternative to experimental research to reduce costs in equipment and energy (Ferzinger and Peric, 2002).

2.3.1 Simplified Mathematical Models for Fluid Flows

The fluid flows found in the real case are governed by the complete Navier-Stokes equations (Anderson, 2017). However, several simplifications to these equations can be done in order to solve the fluid under certain circumstances. The simplified flows that are relevant for the thesis and the general flutter analysis methods are the inviscid (Euler) flow and potential flow.

Inviscid (Euler) Flow

An inviscid flow is that in which viscous, thermal conduction and diffusion effects can be neglected. It is a flow in which the boundary layer is neglected (Anderson, 2017). From the original Navier-Stokes equations the Euler equations are derived for steady, inviscid and without body forces flows (Anderson, 2017). The Euler equations can be seen for the three spatial components in Equation 2.23.

$$\nabla \cdot (\rho u_i U) = -\frac{\partial p}{\partial x_i} \tag{2.23}$$

In which u_i represents each of the velocity components for the different coordinates in space and x_i is the spatial coordinate in each of the 3D coordinates and the index i indicates the coordinate in which the equation is formulated.

Potential Flow

In addition to the assumption of inviscid fluid an irrotational velocity field must be fulfilled for potential flow (Ferzinger and Peric, 2002). This means that the condition $\nabla \times U = 0$ is necessary and a velocity potential ϕ is defined such that $U = \nabla\phi$ (Anderson, 2017). Meaning that potential flow is governed by the Laplace Equation (Anderson, 2017). It can be seen in Equation 2.24.

$$\nabla^2\phi = 0 \tag{2.24}$$

A line of constant ϕ is an equipotential line (Anderson, 2017). Equipotential lines are perpendicular to streamlines for two-dimensional flows (Anderson, 2017). Streamlines are defined as tangent to the velocity vector (Anderson, 2017). The DLM can be found as an application of the potential flow, which needs further corrections to take into account viscous effects.

2.3.2 Turbulent Flow Modelling

Particles contained in turbulent flows behave in a chaotic manner and follow complex irregular paths (Blazek, 2015). This type of flow starts to appear for $Re > 2000$. This relation with

the Re is given by its definition, giving that the relative importance of inertia forces is higher than the viscous forces (Versteeg and Malalasekera, 2007). The chaotic fluctuations in a turbulent flow are deterministic, but the difficulty to model the direct problem (Direct Numerical Simulation (DNS)) is given by the computational effort requirements for $Re > 10^5$ (Blazek, 2015).

The need of an approximate solution for the different effects of turbulence has led to the development of a variety of turbulence models (Blazek, 2015). A diagram of the turbulence model classification based on the one seen in the work done by Blazek (2015) is seen in Figure 2.8.

The classification done is based on the level of modelling performed in each type of model. With increasing level the turbulence modelling is also increased in this scheme. The DNS, the Large-Eddy Simulation (LES) and the Reynolds-averaged Navier-Stokes (RANS) models can be found with increasing turbulence modelling in the diagram.

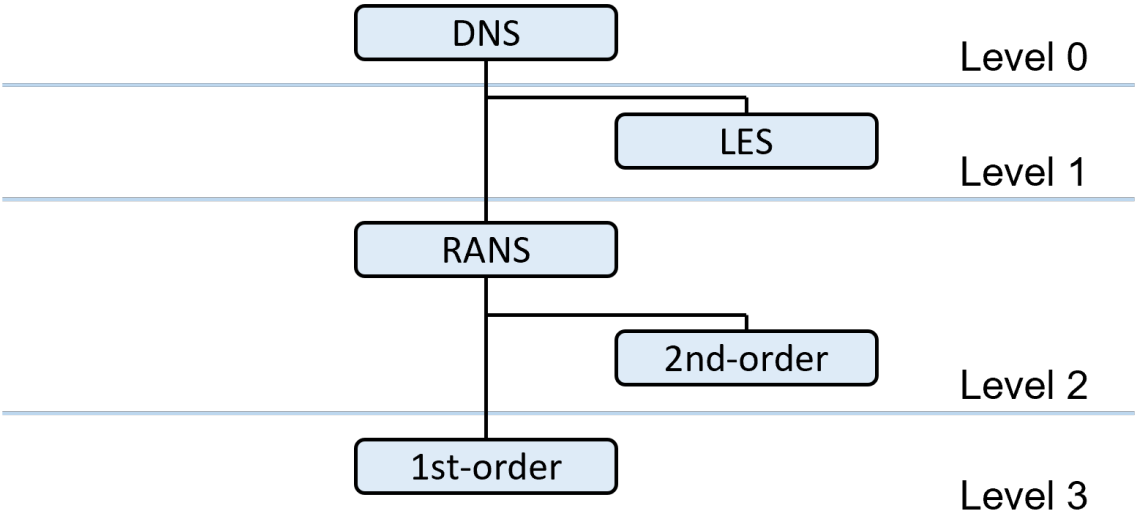

Figure 2.8: Diagram indicating the hierarchy of turbulence models based on the one by Blazek (2015)

The main characteristics of the two main types of turbulence modelling are briefly explained.

Large-Eddy Simulation (LES)

The division of turbulence in different length scales provides the possibility of modelling the decreasing length scales in alternative ways. LES are based in the ubiquity of small turbulent structures, which can be modelled simultaneously solving the larger scales directly (Blazek, 2015). LES provide a time dependant solution in 3D with a computational cost which is signif-

icantly lower than than DNS, but it needs a high grid resolution when compared to the RANS models (Blazek, 2015).

Reynolds-Averaged Navier-Stokes Models (RANS)

Turbulent flows can be treated as a decomposition of a mean and a fluctuating part (Reynolds, 1895). After considering an incompressible flow the expressions seen in Equation 2.25

$$u_i = \overline{u_i} + u_i', \qquad p = \overline{p} + p' \tag{2.25}$$

Where the averaged velocity term is $\overline{u_i}$ and the fluctuating part of the velocity is u_i'. The same indexes apply for the pressure, being $\overline{p}$ the averaged pressure and p' the fluctuating pressure.

RANS models are based on the solution of the fluid only for the mean term. The average can be done temporally, spatially or in an ensemble manner depending on the assumptions done for the flow, being the flow steady or homogeneous (Blazek, 2015). Among the RANS models the most widely-used are the Spalart-Allmaras, the $K-\epsilon$ and the $K-\omega$ SST models (Blazek, 2015).

If a RANS model is extended to perform calculations over time for a given motion, the averaged equations are solved for each timestep in an ensemble averaging (Ferzinger and Peric, 2002). This is known as an Unsteady Reynolds Averaged Navier-Stokes (URANS) model.

2.3.3 Numerical Grid

In order to perform the calculations for the fluid solution, a numerical grid or mesh has to be generated (Ferzinger and Peric, 2002). The variables necessary are computed in a discretized domain, in a finite number of cells. For a Finite Volume (FV) method they are called control volumes (CV). At the centroid of each control volume there exists a computational node and the solution at the surface of the CV is computed by interpolation between nodes (Ferzinger and Peric, 2002). This solution is obtained by applying the conservation equations to every CV.

3 State of the Art

In this chapter a quick overview of the history of flutter is presented in order to understand the present situation. After, the current methods for dealing with this phenomenon are presented.

3.1 Historic Overview of Flutter

The destructive phenomenon of flutter is of interest to the international aeronautic community since the 20s of the last century (Collar, 1978). The natural evolution of science and technology allows different approaches when solving the well known aeroelastic problem. During the 1920s most of the analysis done depended on wing tunnel and experimental testing. In the 30s the development of the Theodorsen tabulated functions the 2D problem is described with additional detail to the previous work done (Collar, 1978). With the potential theory, the Doublet Lattice Method was developed for subsonic oscillating wings in 1968 by Albano and Rodden (1969). In the work done by Giesing et al. (1976) the DLM and wind tunnel testing are mentioned to assess the aerodynamic characteristics of the aircraft. In the early 90s, the DLM is still one of the main tools to assess flutter, as CFD requires a much higher computational cost (Blair, 1992). In the Advisory Group for Aerospace Research & Development (AGARD) report of 1997 (AGARD 1997) CFD is now mentioned as a 'future hope holder' for unsteady aerodynamics predictions. By the beginning of the new century, CFD is still described as a complementary tool and it appears as coupled with the flexible structure of the aircraft (Palacios et al., 2001). As the evolution of computer technology and the ability to perform greater amounts of computations develop, CFD becomes used more often in flutter analysis and unsteady aerodynamics predictions.

3.2 Current Methodologies

To the current date, flutter analysis is not commonly performed by a fully-coupled solution of the elastic, inertial and aerodynamic problems due to the computational cost. However,a feasible outline in the later 2010s and early 2020s is the use of loose-coupling of FEM and CFD models such as in the work done by Rozov et al. (2017). Nevertheless, FEM and CFD are mentioned continuously through this same period of time such as in the studies done by Yao and Marques (2017) and Quinlan and Gern (2018).

The tools mentioned in the previous paragraph are still under development and are not used to completely determine the flutter characteristics of the aircraft under study. They are described as correction or complementary tools to the DLM as of a higher fidelity method that still needs experimental validation through wind tunnel testing and Ground Vibration Tests (GVT). A di-

agram with the main tools for assessing the flutter problem to reach the certification of the aircraft is seen in Figure 3.1.

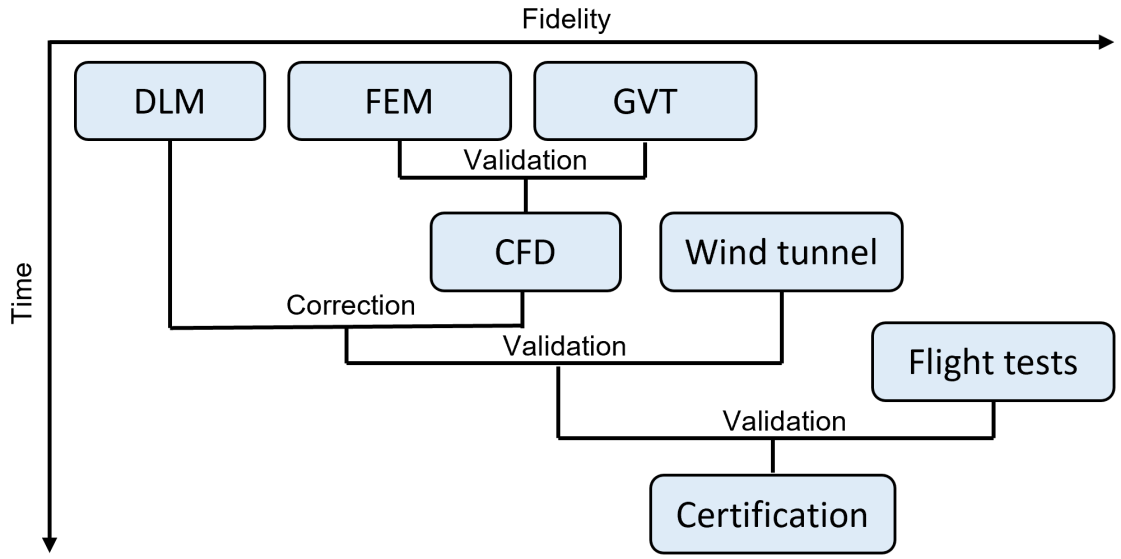

Figure 3.1: Diagram of the tools included in flutter analysis

In this diagram the relation between the different methods for obtaining the aeroelastic behaviour of the aircraft is reviewed. A qualitative description of fidelity is shown, in which lower fidelity methods appear to the left of the diagram while higher fidelity methods are shown to the right. Time is also depicted in the process of certification of the aircraft. An event taking place lower in the diagram happens later in the design process of the aircraft.

This thesis is situated in the CFD block, which is coupled with the FEM block for obtaining the aerodynamics of the aircraft, that will be later used to correct the DLM results.

4 Methodology

This chapter describes the single steps to setup and run the unsteady simulations performed in the scope of this thesis. We can distinguish the Computer Aided Design (CAD) preparation and the numerical setup. The process of the geometry completion and modification is done by means of CATIA V5R21. The numerical setup includes the mesh generation and its verification, the setup for the simulation, the coupling with the FEM solution for the morphing of the wing and the convergence analysis of the unsteady solution. The processes of mesh generation and fluid solution are performed in STAR-CCM+. An unsteady-state simulation is performed for each combination of vibration mode and reduced frequency.

4.1 Geometry Completion and Modification

The geometry used is the right wing of the reference aircraft. It is divided in six sections with a flap in each of them. The dihedral angle increases spanwise to have higher stability. In a previous study by Rambla Areal (2022) the winglet was neglected, as it can be seen in Figure 4.1.

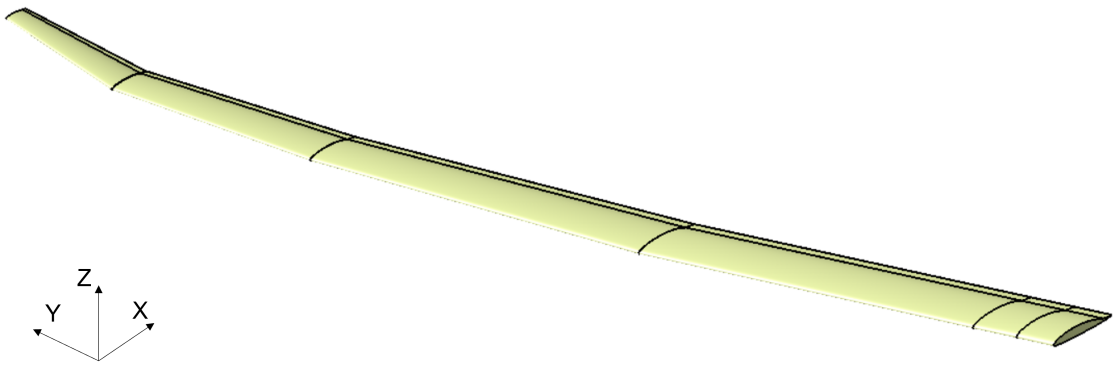

Figure 4.1: Initial geometry. Tip to root from left to right

In the scope of this thesis the winglet is considered as well. The geometry of the winglet is provided by the manufacturer. In the original geometry, the joint of the winglet and the wing does not match both sides perfectly, which can cause skewed cells to appear during the meshing process. To avoid these skewed cells, which can cause numerical instabilities, the geometry near the joint is slightly modified and smoothed. The difference in the provided winglet geometry and the modified geometry can be observed in Figure 4.2.

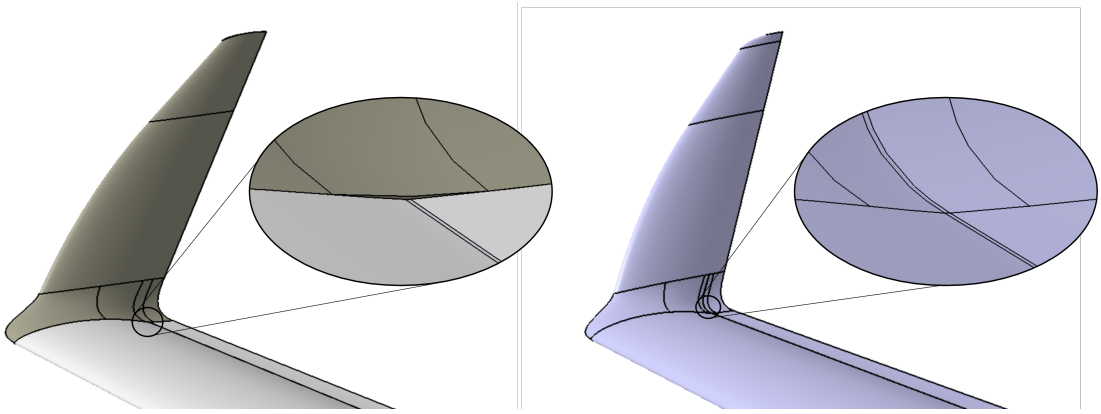

Figure 4.2: Winglet before and after its modifications

The modifications done are assumed to be of minor influence in the aerodynamics of the wing.

4.2 Mesh Generation

The mesh generation is divided in two steps; one for the main wing and one for the winglet. The mesh at the wing was generated by Rambla Areal (2022). The mesh at the winglet is studied to perform a mesh independence analysis.

4.2.1 Wing Mesh

The unstructured mesh used for the simulations is based on the mesh independence study performed by Rambla Areal (2022) for the SA turbulence model. In this case the wake refinement is removed to reduce the computational effort, as it is not in the scope of this thesis to study the wake generated after the wing, it is centered in the forces in the Z coordinate. This mesh with prism layer is optimized to compute the solution for $Re = 2e6$. The fine discretization of the prism layer is used to capture the boundary layer and the viscous effects. For the cases in which the Re are higher, the boundary layer is still captured completely, but the $y+$ is not under the desired value of 1. It reaches values of 1.44. The same way, at lower Re the $y+$ is kept under 1, but the boundary layer is thicker than the prism layer. In both cases the mesh should be adapted to the different fluid conditions, but the range of $3e5 < Re < 4e6$ would require several meshing procedures. In the scope of this thesis the mesh optimized for $Re = 2e6$ over the wing is used for all cases. The mesh of the wing can be seen in Figure 4.3 with a section displayed next to it.

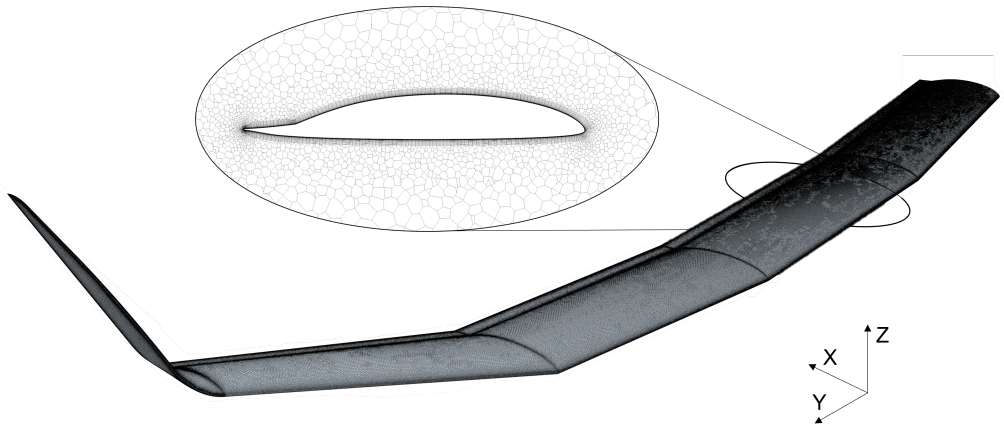

Figure 4.3: Overall mesh with a section detail

4.2.2 Winglet Mesh

The base mesh generated for the wing is extended and modified in the winglet region. The characteristic length selected to determine the prism layer parameters (number of prism layers, prism layer near wall thickness and prism layer total thickness) is the chord of the winglet. The Re in this area is lower due to the shorter chord length. A mesh independence procedure is performed for the winglet region. Different refinements over the winglet are analysed in order to choose the mesh size with the best relation of computational effort against variation of the C_L and C_D, which must fall to 1% to consider it acceptable. This variation has to be achieved between meshes with increasing number of cells.

Winglet Near Field Surface

The field near the winglet is a subdomain described by a truncated cone containing the geometry. It serves as transition from the farfield coarse mesh to the finer mesh close to the walls. The size of the cells in this region is defined by the characteristic length of the cells in the surface of the subdomain. Table 4.1 gathers the data from the mesh independence in this zone.

Table 4.1: Winglet near field surface mesh independence

Characteristic length [m]	Cell count	C_L	Variation [%]	C_D	Variation [%]
0.05	37969663	0.396110	base	0.0136569	base
0.025	37970125	0.396125	0.004	0.0136631	0.05

Winglet Surface

In the prism layer, the size of the cells in the fluid direction that defines its aspect ratio. Defined by its size as a percentage of the base size. The characteristic length is selected to be the length of mean aerodynamic chord (c_{MAC}). In Table 4.2 the parameters for the mesh independence study in this zone are observed.

Table 4.2: Winglet surface mesh independence

Characteristic length [%]	Cell count	C_L	Variation [%]	C_D	Variation [%]
1	37170911	0.396115	base	0.0136554	base
0.75	37447173	0.396110	0.001	0.0136546	0.006

LE and TE Volumes

Due to the presence of significant gradients of fluid state variables in the LE and TE zones, a refinement must be preformed. A volumetric control is used and cells are defined by its size as a percentage of the base. In Table 4.3 the mesh independence results are displayed.

Table 4.3: LE and TE volumes mesh independence

Characteristic length [%]	Cell count	C_L	Variation [%]	C_D	Variation [%]
0.2	37969663	0.396110	base	0.0136569	base
0.15	38416828	0.396105	0.001	0.0136578	0.007

TE Surface

The TE is a zone with sharp edges close to each other. For this reason, it needs to have a refinement to achieve a certain discretization over its surface. A refinement of at least five cells is desired. The cell size is defined by its size as a percentage of the base. In Table 4.4 the results regarding this refinement are shown.

Table 4.4: TE surface mesh independence

TE Surface [%]	Cell count	C_L	Variation [%]	C_D	Variation [%]
0.05	38142468	0.396110	base	0.0136573	base
0.025	38584541	0.395912	0.05	0.0136513	0.04

4.3 Steady-State Convergence of the Mesh

The steady-state solution is evaluated in each of the cases separately in order to reach convergence of each mesh. The convergence is evaluated by means of three different methods: residuals, variation of critical parameters and fluid observation based on scenes.

4.3.1 Residuals

The turbulence model employed to take viscous effects into account is the Spalart-Allmaras Model. With this model five different residuals are evaluated. Three parameters describe the fluid momentum in the coordinate system directions (X, Y , Z), one describes mass continuity throughout the domain and one last residual the SA parameter. These residuals are expected to fall in the order of magnitude of 10^{-6} to reach convergence. With the different meshes the residuals drop to a value in the order of magnitude of 10^{-5} if not below. This convergent behaviour is considered to be acceptable in the scope of this thesis.

4.3.2 Variation of C_L and C_D

For the convergence of the case, the variation of these two non-dimensional parameters is evaluated at each iteration. Both values are expected to reach variations of less than 0.1% in the last 1000 iterations to be considered converged.

4.3.3 Fluid Gradients

Several scenes and scalar values for pressure and velocity distributions are checked over the wing. Spurious behaviours of the fluid are sought, such as considerable pressure gradients or velocity fields in which the direction is unexpected. Not finding any confirms the convergence of the solution.

4.4 Setup of the Simulation

After the implementation of the CAD geometry in the CFD software and the spacial discretization of the domain, the different boundary conditions and solver models are applied to perform the simulation and obtain a converged solution for the different flight velocities.

4.4.1 Domain Description

The domain of the simulation is based on the one proposed by Rambla Areal (2022). The domain is extended in all directions consisting in 150 chords downstream to allow the flow to develop, 40 chord lengths upstream and 60 chord lengths in the lateral width of the domain. The domain can be seen in Figure 4.4. In this case the boundary condition for the wall in which the wing is fixed is also modified to be a symmetry plane.

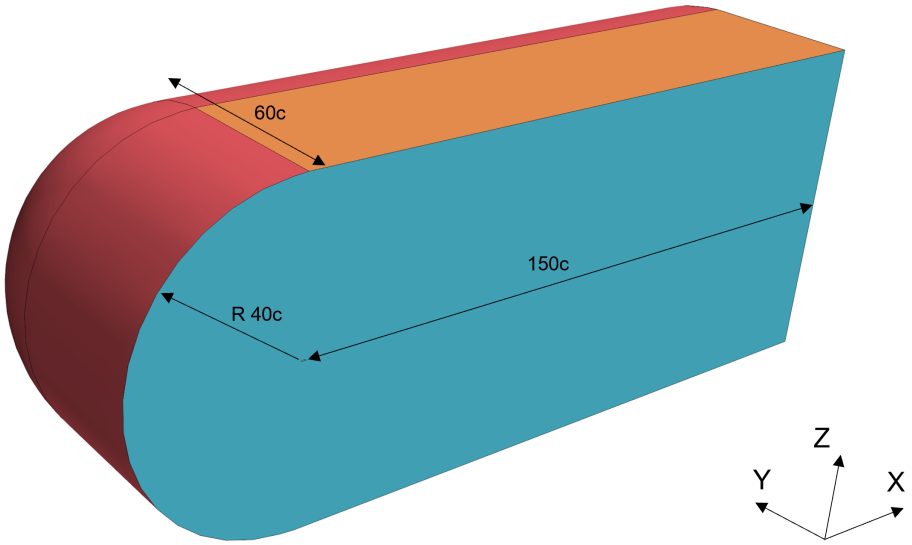

Figure 4.4: Computational domain; blue wall represents symmetry plane, orange for pressure outlet and red for velocity inlet

4.4.2 Boundary and Initial Conditions

It is assumed that the aircraft is flying in cruise conditions at Mean Sea Level (MSL) and Iternational Standard Atmosphere (ISA) conditions for the free-flow properties. This translates as the velocity being measured as the (Equivalent Air Speed) EAS. Further corrections should be applied to air density and compressibility for real flight conditions. These corrections to obtain the True Air Speed (TAS) for an incompressible flow can be done by means of Equation 4.1. As the aircraft is assumed to be in cruise conditions for every case, an angle of attack $\alpha = 2°$ is chosen.

$$U_{TAS} = U_{EAS}\sqrt{\frac{\rho_{MSL}}{\rho}} \tag{4.1}$$

The values of the flight conditions considered are found in Table 4.5 and are common to every case studied.

Table 4.5: Free flow conditions for the studied cases

Pressure, p_∞	Air density, ρ_∞	Dynamic viscosity, μ_∞	Temperature, T_∞
101325 Pa	1.225 kg/m^3	1.812e-5 Pa·s	288.15 K

These parameters serve as initial conditions for the flow together with the velocity vector. The magnitude of the velocity ranges from $7.74\ m/s \leq U_\infty \leq 100\ m/s$. Therefore, the

range of Mach numbers is $0.02 \leq Ma_\infty \leq 0.29$, meaning that compressibility effects can be neglected. The solver is set to segregated for the velocity and the pressure. A segregated solver has its roots in constant-density flows and employs a predictor-corrector method for solving the continuity and momentum equations. Pressure as a variable is obtained from the pressure-correction equation (Siemens, 2021).

4.4.3 Steady-State Convergence of the Cases

For each of the velocities the same methods as for the mesh independence are used to assess convergence. Convergence criteria are met under every requirement except for $y+ < 1$, which was expected for the highest velocities and reaches values of 1.44 for the highest Re. This value depends on the mesh used. As previously stated, the mesh is kept constant through the whole range of Re in the scope of the thesis.

4.5 Coupling with the FEM Modal Analysis

In order to perform the unsteady simulation, the oscillating vibration of the wing is applied to the geometry. In the scope of this thesis the unsteady simulations are performed considering harmonic oscillations of the wing that may occur at the flutter boundary. The geometrical perturbations are considered by means of a loosely-coupled simulation with the FEM results of a modal analysis of the wing. The FEM modal analysis results were obtained and validated with a GVT by Mendl (2022). These results are presented in a Nastran output file obtained with 'SOL 103 NASTRAN Modal Analysis'. The structural mode shapes are described with eigenvectors and eigenfrequencies at the FEM beam nodes. The FEM model is imported into the CFD software. The complete spectrum of vibration modes provided by the FEM solution is to be analysed in a process chain. In this work only two of the modes are studied due to time limitations. These two modes are the first symmetric wing bending oscillation (S1) and the symmetric fuselage bending of two static nodes (SR2). The eigenvectors defining each mode can be seen in Figure 4.5.

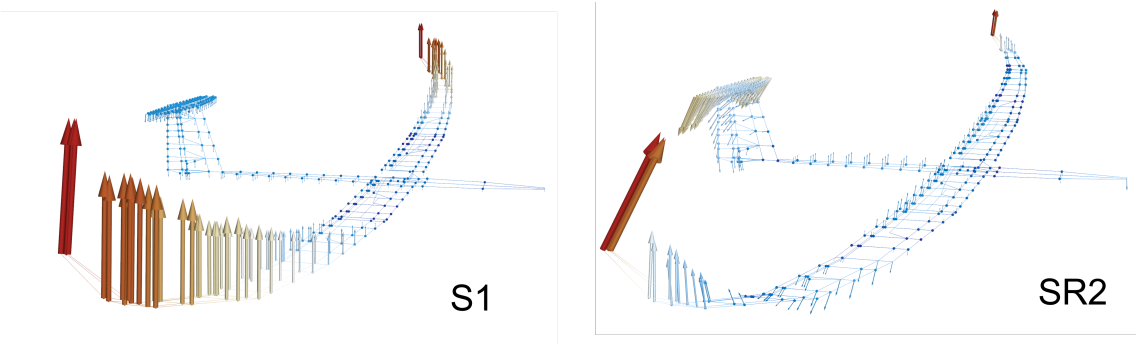

Figure 4.5: Vibration modes analysed, normalised to the maximum displacement

4.5.1 Velocities Selection

In order to study the different reduced frequencies for S1 and SR2, critical points in the Theodorsen Function (see Figure 2.5) are chosen within the flight envelope. These are the values of $k = 0.1, 0.3, 0.6$. These points are situated before, in and after the maximum phase shift. The chord length c_{MAC} is fixed for the aircraft and the frequency of oscillation is defined by the studied mode. The velocity varies in the reduced frequency in Equation 4.2.

$$k = \frac{\omega_r c_{MAC}}{2U_\infty} \tag{4.2}$$

The flight envelope of the aircraft does not cover the velocity which corresponds to $k = 0.1$ for SR2. A maximum velocity reachable for the reference aircraft is studied instead, $100\ m/s$. The reduced frequency of $k = 0.6$ is not a flight velocity for this aircraft, nevertheless a range of the velocities described by the manufacturer for the aircraft is of $1\ m/s \leq U_\infty \leq 100\ m/s$. The velocities and reduced frequencies for each case are shown in Tables 4.6 and 4.7.

Table 4.6: Velocities and reduced frequencies for S1

S1, $f = 2.35$ Hz			
k	0.1	0.3	0.6
U_∞ [m/s]	46.46	15.49	7.74

Table 4.7: Velocities and reduced frequencies for SR2

SR2, $f = 12.61$ Hz			
k	0.25	0.3	0.6
U_∞[m/s]	100	83.92	41.96

4.5.2 Motion Modelling

The structural deformation is assumed to follow an harmonic sinusoidal oscillation. Each of the nodes in the beam model translates to its next position in the unsteady setup following Equation 4.3. The displacement $u(t)$ of every node is represented in Cartesian coordinates. This harmonic oscillation corresponds to a structural deformation that may occur at the flutter boundary.

$$u(t) = \Phi \cdot q_r(t) = \Phi \cdot \frac{A}{|\Phi_r|_{max}} \sin(\omega_r t) \tag{4.3}$$

The eigenvector matrix (Φ) is normalised with the maximum displacement of the vibration mode applied to the structure $|\Phi_r|_{max}$. Here $q_r(t)$ represents the vector of displacements in modal coordinates applied to the structure. Only one vibration mode is applied. They are weighted to have a maximum amplitude of A of 5 mm, approximately 1% of the c_{MAC}. This limitation is chosen in order to stay in the linear aeroelasticity (Förster, 2016).

4.5.3 Morpher Solver

A mapping from the beam model to the walls of the CFD model is performed. This allows the interpolation of the node displacements to the whole wing surface and the mesh. This step also requires the highest amount of storage capacity. A finer mesh and more modes result in more data being stored. The displacements are stored in a Point Set, used to describe the mesh deformation.

The BSpline morpher is chosen. It progressively refines the control-point grid until the residual error is within the limits specified by the morpher tolerance (Siemens, 2021). This tolerance is set to be of 10^{-10}. It allows sufficiently accurate morphing of the domain. In the morphing solver, the Morph from Zero option is checked. It gives repeatable meshes for periodic morphing such as the one performed in an oscillating element. Boundary Layer Morphing is checked to make sure only the walls of the wing and winglet are morphed. The Recompute Interfaces option is selected to make sure that the interfaces between cells are well computed at every timestep.

4.5.4 Post-Processing of the Loosely Coupled Simulation

The friction and pressure forces are integrated over the wing to obtain the total forces acting on it. The wall shear stress and the pressure coefficient are computed in each cell on the walls. Equations 4.4 and 4.5 show respectively the friction ($F'_{f,r}$) and pressure ($F'_{p,r}$) forces

equations for the n number of wall cell i. The subindex r represents the oscillation mode deforming the wing. The expressions for the forces obtained do not have the dimension of a force due to the normalisation with the dynamic pressure. This is expressed with the prime symbol (').

$$F'_{f,r} = \frac{1}{q_\infty} \sum_{i=1}^{n} |S_i| \cdot \tau_i \tag{4.4}$$

$$F'_{p,r} = \sum_{i=1}^{n} c_{p,i} \cdot S_i \tag{4.5}$$

The wall shear stress is dimensionalised with the dynamic pressure to have the same dimensions as the pressure coefficient. It is multiplied by the magnitude of the area of each cell, the direction is parallel to the flow in that cell. The pressure coefficient is multiplied by the normal vector to the area of the wing. When summed up together the total forces (F'_{Tr}) over the wing are obtained as seen in Equation 4.6.

$$F'_{T,r} = F'_{f,r} + F'_{p,r} \tag{4.6}$$

Total forces over the wing in Cartesian coordinates are multiplied by the matrix of eigenvectors in Equation 4.7. The generalized forces are obtained. Every combination of mode applied to the wing, in the scope of this thesis S1 and SR2, with a non applied mode (j) results in the elements of the generalized forces.

$$f_{gen,r} = \Phi^T \cdot F'_{Tr} \tag{4.7}$$

In the flutter analysis S1 would represent the theoretical 2D flutter case described in Section 2.1.2, in which the bending couples with the torsion (Bisplinghoff et al., 1996). The mode SR2 is chosen based on a real case of flutter, this mode coupled with the symmetric wing bending oscillation of third frequency (S3) at high flight velocities. Here a maximum velocity of $100\ m/s$ is studied and compared with lower speeds. The elements in the generalized aerodynamic forces (GAF) matrix are obtained. Each term GAF_{rj} is a complex quantity representing the magnitude and phase of the force $f_{gen,rj}$, as shown in Equation 4.8. Given that q_0 is the flutter solution displacement for the motion equation in the frequency domain.

$$f_{gen,rj} = q_\infty GAF_{rj}(k) \cdot q_0 \tag{4.8}$$

The objective of this work is the obtention of the GAF elements and being able to compare them with the DLM solution. The methodology will be later incorporated into a process tool chain.

4.6 Unsteady-State Convergence

The steady solution is the starting point of zero displacement for the unsteady solution. A variation of less than 1% in C_L and C_D in between consecutive oscillating periods is sought. For the case of S1 with $k = 0.1$, five periods were reached for a consistent convergence without an exceedance in computational effort. A number of 100 timesteps per oscillation period and 20 inner iterations in each timestep are needed to achieve the desired accuracy. Five periods of 100 timesteps per period and 20 inner iterations per timestep were standardised to assess convergence. An additional period of 200 timesteps is run afterwards to check time discretization.

5 Results

The analysis of the results of the CFD simulations is divided in the two modes studied. The behaviour of the main aerodynamic coefficients C_L and C_m are thoroughly explained in the context of each mode. The C_D could also be examined in detail, but the results regarding this coefficient are dismissed. They do not have a considerable impact on the studied flutter modes. The direction of the drag forces is quasi-perpendicular to the eigenvectors of the modes, meaning that almost no influence is expected. The plots regarding this coefficient are displayed in Appendix A.

The main generalized forces for each vibration mode are analysed. The process to obtain the elements of the GAF matrix is also explained and an example of how to obtain them is performed. Due to the high amount of post-processing operations needed to perform this task, the use of macros in STAR-CCM+ is necessary. Macros used for the pre and post-processing have been used throughout the simulations. Some of the macros employed can be seen in Appendix B.

Mode S1 does not converge for the $k = 0.3$ and the proposed setup. A refinement process regarding timestep and inner iterations is done. After several iterations no conclusive results are obtained. The plots regarding the combination of S1, $k = 0.3$ are found in Appendix C.

5.1 Mode S1

The wing bending oscillation can be approximated to the 2D plunging case. This approximation is valid due to the eigenvectors of the mode being almost vertical and due to no variation of magnitude chordwise. This means that the displacement is only dependent on the position spanwise and every section of the wing behaves as a 2D plunging. The eigenvectors can be seen in Figure 5.1.

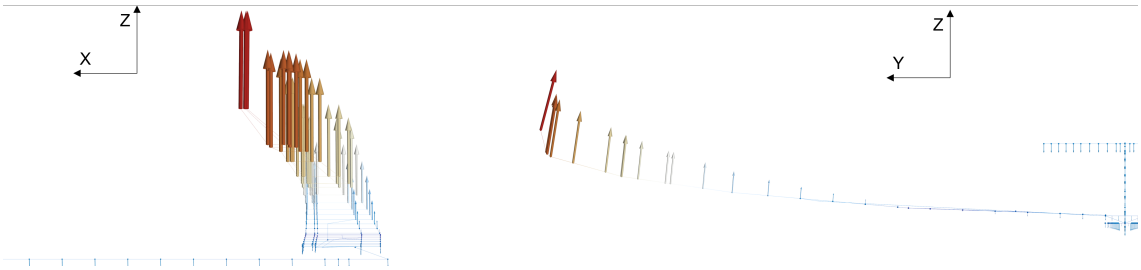

Figure 5.1: Lateral and front view of the mode S1

For a better understanding of the behaviour of the motion, a visualisation of the evolution of the velocity of the wing over time can be seen in Figure **??**.

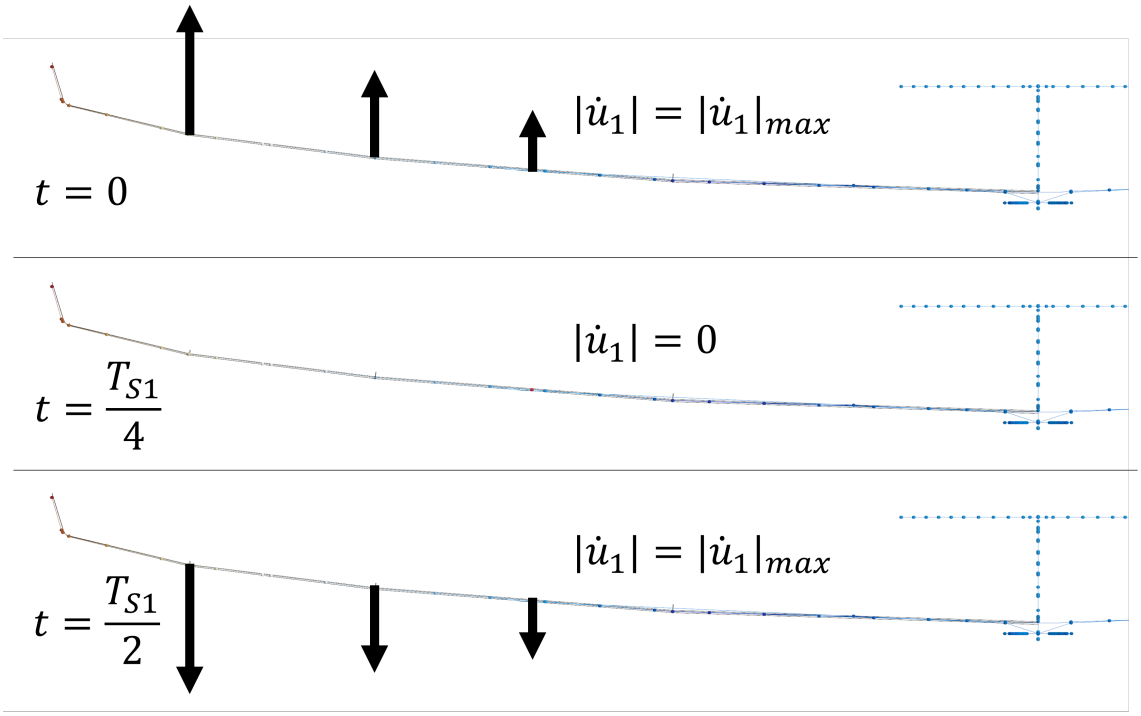

Figure 5.2: Evolution of the velocity associated to S1 with time

These fluctuations in the velocity evolve as a cosine function due to it being the derivative of the position. The different coefficients and results for this motion are studied in the following sections.

5.1.1 Theoretical Variation of C_L for S1

The motion of the case studied can be assumed to be a purely a bending case. The unsteady lift Equation 2.16 can be simplified to only be function of u_1 and its derivatives and k. The plunging (u_1) and torsion (u_2) coordinates can be visualised in Figure 5.3.

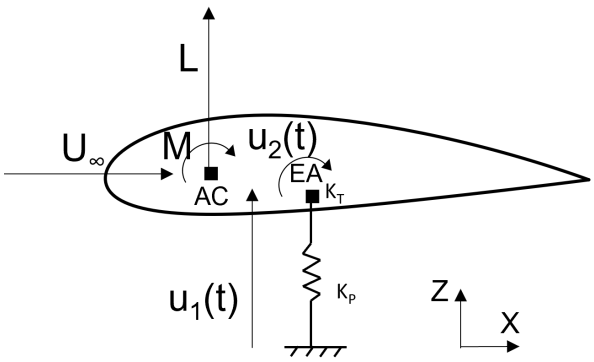

Figure 5.3: 2D coordinates for plunging and torsion

This simplification is seen in Equation 5.1. This lift equation holds for a section of the wing and is computed per unit span for an average displacement at the c_{MAC}.

$$\Delta L' = qC_{l\alpha}c \cdot \frac{c\ddot{u_1}}{4U_\infty^2} + qC_{l\alpha}c \cdot C(k) \cdot \frac{\dot{u_1}}{U_\infty} \tag{5.1}$$

The equation is dimensionless and the C_L is as shown in Equation 5.2.

$$\Delta C_L = C_{l\alpha} \cdot (\frac{c\ddot{u_1}}{4U_\infty^2} + C(k) \cdot \frac{\dot{u_1}}{U_\infty}) \tag{5.2}$$

The theoretical C_L for $k = 0.1$ is now computed for the c_{MAC} and it is compared to the CFD values. The same procedure can be followed for the rest of reduced frequencies in S1. In Equation 5.2 the positive direction for the displacement u_1 is downwards. As seen in Figure 5.3 the displacement is considered positive upwards in the scope of the thesis. Therefore the displacement must be multiplied by -1 to behave as expected. The displacement is computed as seen in Equation 5.3.

$$u_1(t) = -\frac{|\Phi_{MAC}|}{|\Phi_{S1}|_{max}} A \sin(\omega_{S1} t) \tag{5.3}$$

The values of the constants involved in equations 5.2 and 5.3 for lift computation are shown in Table 5.1.

Table 5.1: Constants for theoretical lift at the MAC for S1, $k = 0.1$

Constant	Value
$C_{L\alpha}$	5.214/rad
c	0.635 m
U_∞	46.46 m/s
$C(k)$	0.83192-i0.17230
$\|\phi_{MAC}\|$	0.1484 m
$\|\phi_{S1}\|_{max}$	1.03 m
A	0.005 m
ω_{S1}	14.77 rad/s

The values come from different sources. $C_{L\alpha}$ is computed from the polar curves obtained

by Rambla Areal (2022). The c_{MAC} is computed from the planform of the wing. The values of the Theodorsen function for $k = 0.1$ are obtained from the tables compiled in (Luke and Dengler, 1951). The magnitude of the eigenvector at the MAC is interpolated linearly from the closest eigenvectors (Φ_+ closer to the wing tip and Φ_- closer to the wing root). The discretization of the wing in the FEM model does not include a node at the MAC. Therefore a linear interpolation is done and the approximate value is obtained. The discretization can be seen in Figure 5.4, where the position of the MAC is represented as a red probe. The horizontal distance between the closest nodes ($y_+ - y_-$) is taken as a reference and given the value of 1. The distance between the MAC and the reference node closer to the wing root (y_{MAC}) has a normalized value of 0.24.

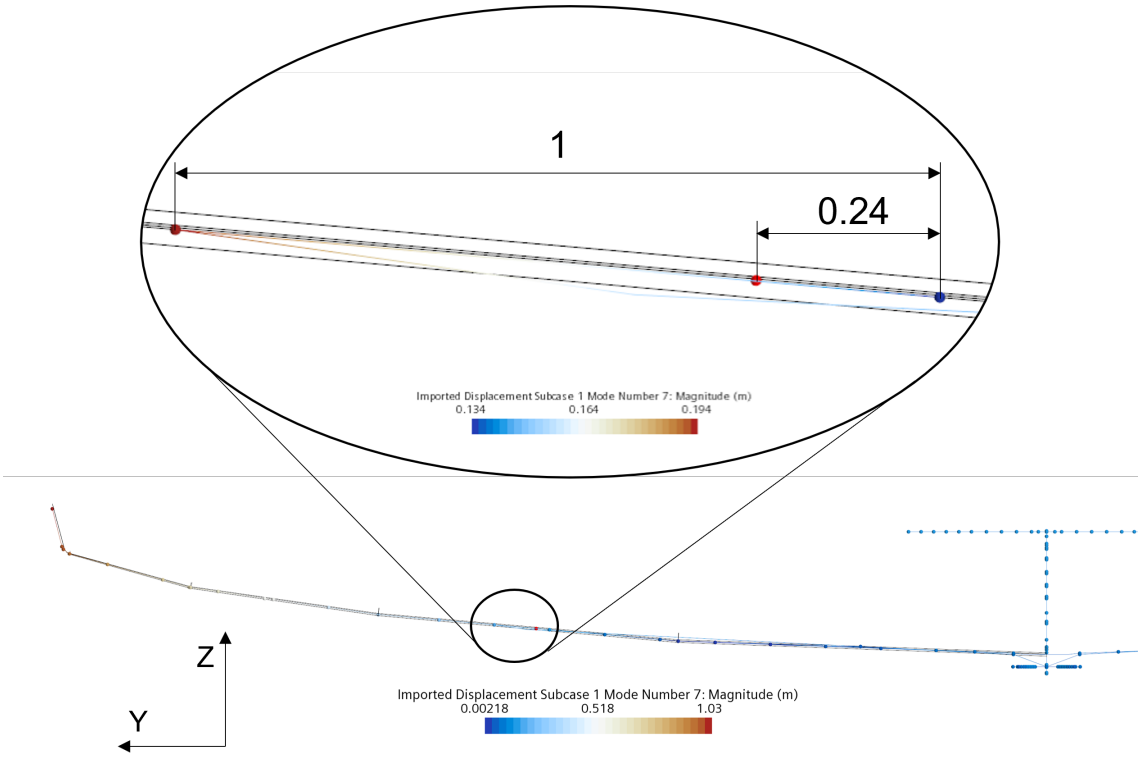

Figure 5.4: Discretization of the wing and eigenvector magnitude around the MAC

From the maximum and minimum values of the eigenvectors and the horizontal distances seen in the detail of Figure 5.4 the linear interpolation done is seen in Equation 5.4.

$$|\Phi_{MAC}| = \frac{|\Phi_+| - |\Phi_-|}{y_+ - y_-} \cdot y_{MAC} + |\Phi_-| = \frac{0.194 - 0.134}{1 - 0} \cdot 0.24 + 0.134 = 0.1484m \quad (5.4)$$

All the constants are known and the solution of the equation for the theoretical lift can be obtained. The obtention is seen in Appendix D. Equation 5.5 shows the solution.

$$\Delta L(t) = 5.214 \cdot (1.1 \cdot 10^{-5} \sin(14.77t) - 1.9 \cdot 10^{-4} \cos(0.2042 - 14.77t)) \tag{5.5}$$

The oscillation occurs around an average lift. This value is obtained from the CFD steady simulation. This value is of $C_{Lavg} = 0.3961$. The theoretical lift is plotted next to the results obtained in CFD in Figure 5.5. The horizontal axis represents the time at the beginning of the seventh period of oscillation.

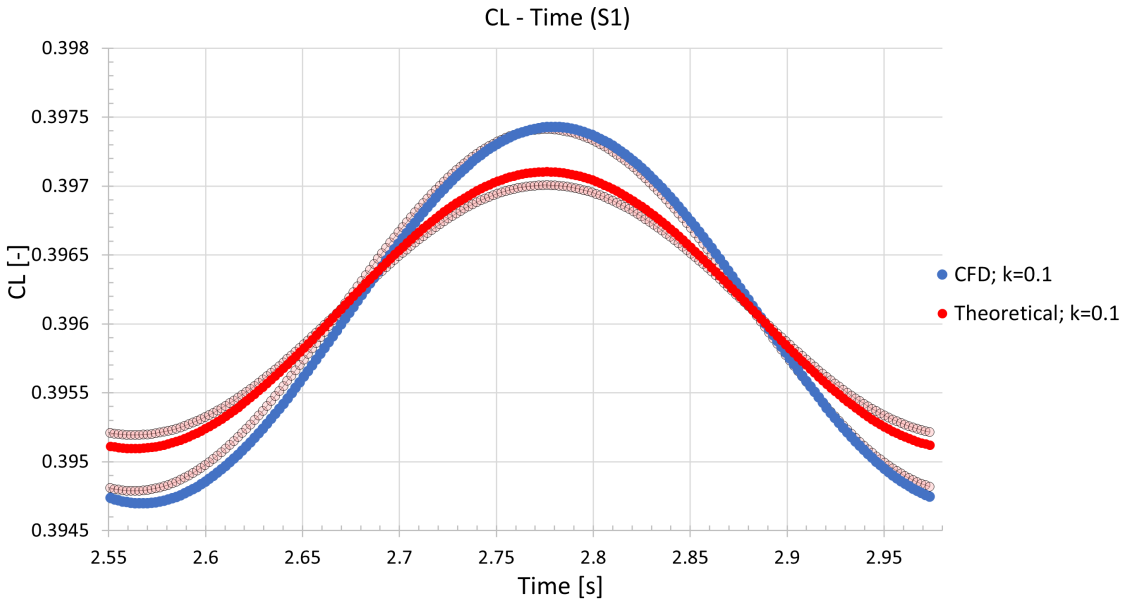

Figure 5.5: C_L obtained from the 2D theory and from CFD results

The red curves correspond to the theoretical values and the blue to the CFD results. Two additional error plots have also been plotted due to the possible deviations in the eigenvector obtention with the interpolation. The eigenvectors used for the maximum and minimum amplitude are the ones placed at the nodes of the FEM model. The oscillations of the theoretical and the CFD-obtained lift are represented as a phased cosine: $C_{Lavg} - B\cos(\omega_{S1}t + \beta)$. Their amplitude and phase can be computed and are compared in Table 5.2.

Table 5.2: Comparison of theoretical and CFD obtained C_L for S1, $k = 0.1$

Constant	Theoretical	CFD	Error
Amplitude (B)	1.004e-3	1.329e-3	32.37%
Phase (β)	-12.600°	-16.215°	3.615°

From the results obtained it can be stated that the theoretical solution applied to the MAC of the aircraft does not provide a reliable solution when compared to CFD in magnitude terms, but it serves as first approximation to analyse the phasing of the lift with respect to the motion of the wing. It must also be mentioned that the considered error due to the interpolation makes the expected values almost fit the CFD results. CFD results take into account the behaviour of the whole wing, not only a section and are more precise. Nevertheless the CFD calculations require a lot of computational effort and long simulation times.

5.1.2 Variations of C_L with k for S1

The C_L function obtained from CFD with the reduced frequency can be defined by the amplitude and the phase. The response of both $C_L(k, t)$ over time can be seen in Figure 5.6.

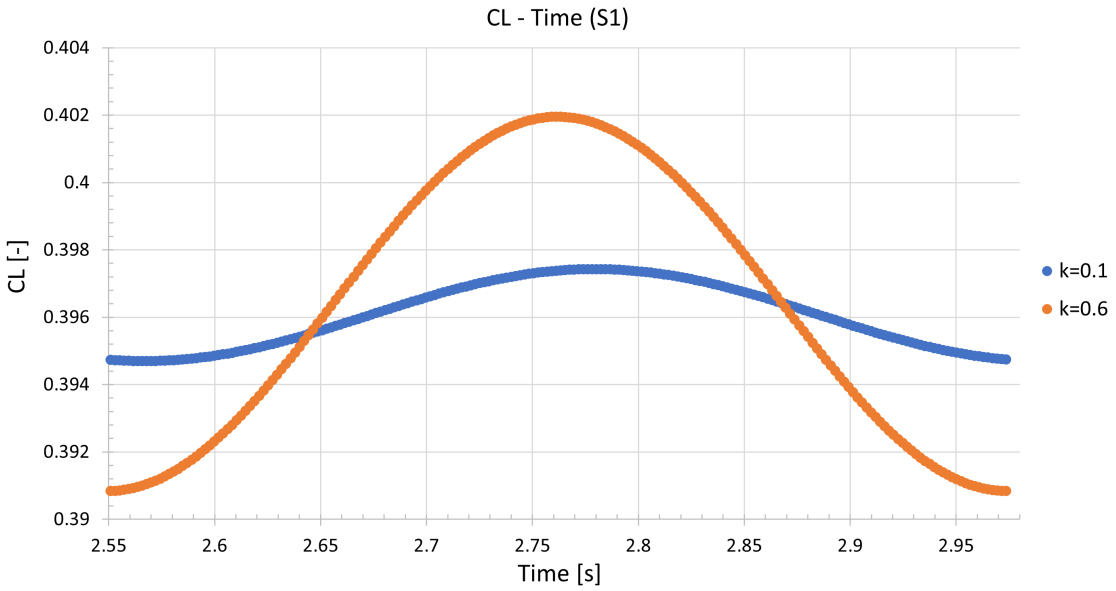

Figure 5.6: Evolution of the C_L for the mode S1 as a function of time

The amplitude and phase of the oscillations due to different reduced frequencies can be obtained as in the previous Section 5.1.1. An extensive quantitative analysis is not performed for the reduced frequency of $k = 0.6$ because of the low free-stream velocity at which the aircraft

is not able to fly. A qualitative analysis is done instead.

The amplitude of C_L at $k = 0.6$ is clearly greater than at $k = 0.1$. This is due to the lower free flow velocity. For a lower velocity, greater angles of attack are felt by the wing during the same oscillation amplitude and frequency. This effect is represented in Figure 5.7

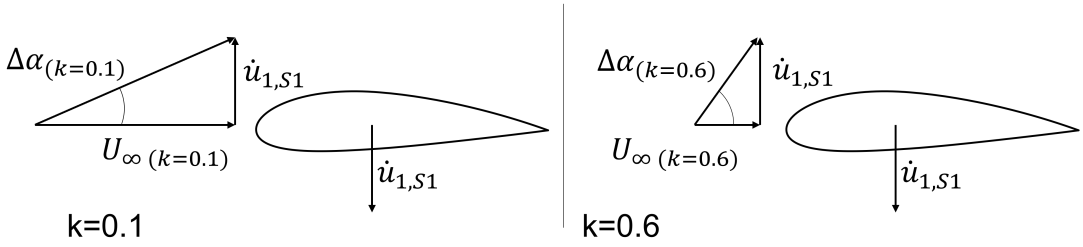

Figure 5.7: Increments in AoA for the different values of k for a plunging mode

The difference in phase can be explained by two factors. The first is the phase predicted by the Theodorsen function, which is greater for $k = 0.6$ than for $k = 0.1$. This is a higher negative phasing. This effect should only account for a difference of around 2° between these two k. The second effect is caused by the free-flow velocity. The oscillation acceleration is divided by the velocity squared in Equation 5.6.

$$\Delta C_L = C_{l\alpha} \cdot \left(\frac{c\ddot{u}_1}{4U_\infty^2} + C(k) \cdot \frac{\dot{u}_1}{U_\infty}\right) \tag{5.6}$$

For lower velocities the effect of the first term is higher. As this term is phased and summed, it adds an additional phasing to the total lift. For $k = 0.6$, both effects have the same value, but in opposite directions. For this reason apparently no phase is seen in the plot. For $k = 0.1$ the effect of the first term is lower, and the Theodorsen phase is kept with more importance. The amplitude of the two terms in Equation 5.5 allows a comparison between terms. The term including the Theodorsen function is an order of magnitude higher than the term with only a real part.

The phasing and amplitude can also be seen in the histeretic plot of the C_L against the maximum displacement found in the wing. This is seen in Figure 5.8.

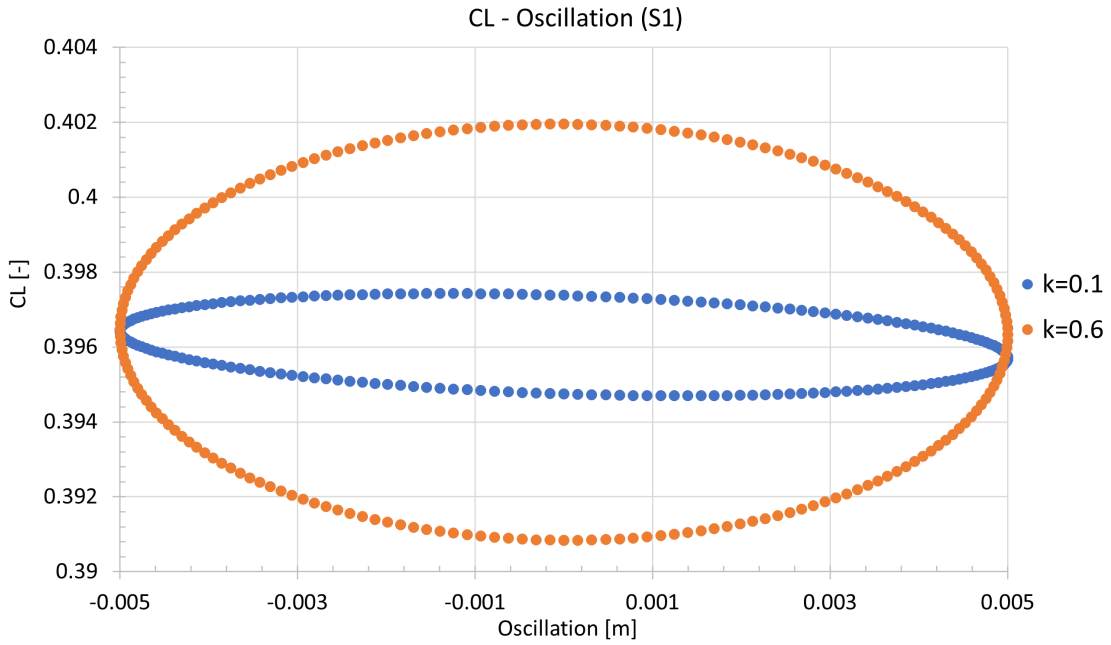

Figure 5.8: Evolution of the C_L for the mode S1 as a function of the oscillation

Amplitude can easily be interpreted as the difference between the highest and lowest point in the ellipses. Phases can be seen in the inclination of the ellipse. For pure bending, a perfectly horizontal axis would mean a phase of zero degrees with respect to the velocity of oscillation. This type of plot is specially useful for assessing the time convergence of the results. Ellipses are plotted one over the other. A better closed ellipse matching the one from the previous oscillation would mean a converged solution over time.

5.1.3 Variations of C_m with k for S1

The behaviour of the moment coefficient around the aerodynamic center is now studied. The aerodynamic center has been assumed to be at the first quarter of the chambered airfoil (Anderson, 2017) at the MAC. Therefore, the axis around which the C_m is computed is placed in this point. The position of the MAC and the C_m axis are seen in Figure 5.9.

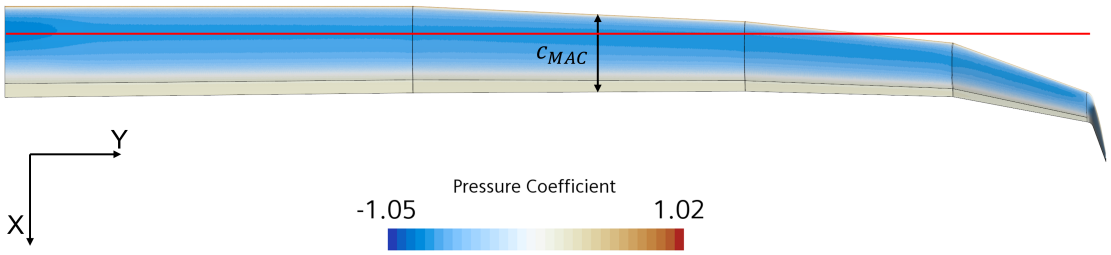

Figure 5.9: Pressure distribution over the wing. Position of the mean aerodynamic chord in black and axis around which C_m is computed in red

As seen in the previous Figure 5.2, the part of the wing which feels greater velocities associated to the vibration is the wingtip. The wingtip is located behind the moment axis, seen in Figure 5.9. For a downwards velocity, at $\frac{T}{2}$, higher increments in the local angle of attack are expected at the wingtip. The evolution of the C_m over time for the two different reduced frequencies is seen in Figure 5.10.

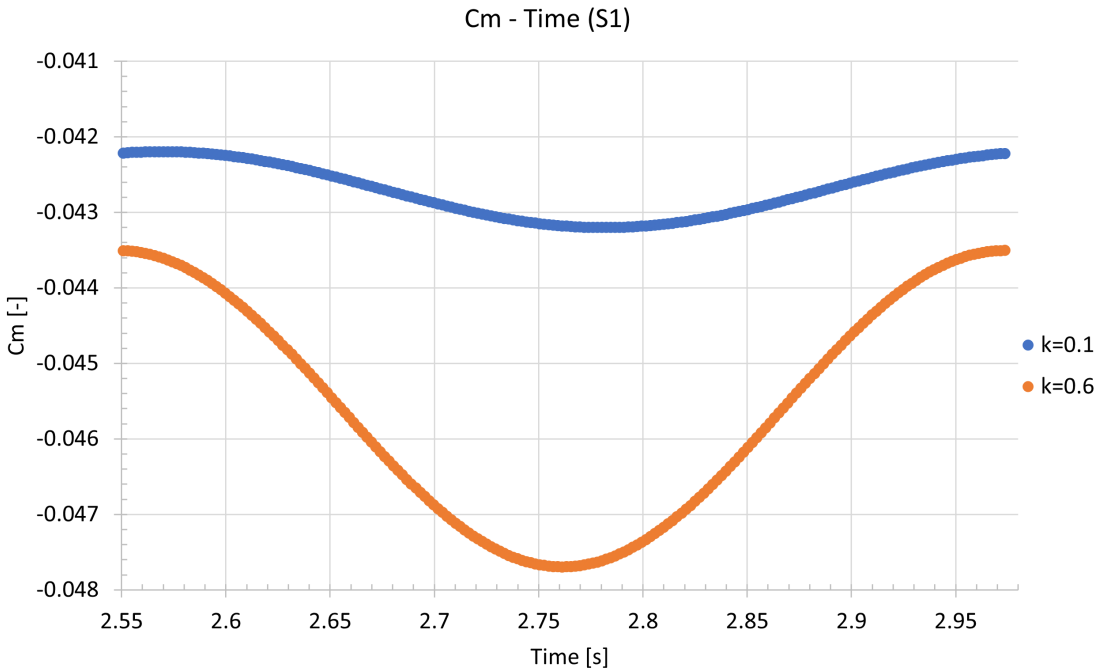

Figure 5.10: Evolution of the C_m for the mode S1 as a function of time

And the C_m can be approximated to a cosine function $C_m = C_{m,avg} + B\cos(\omega_{S1}t + \beta)$ with an amplitude, phase and average value of the coefficient that are seen in Table 5.3.

Table 5.3: Constants for C_m for S1, $k = 0.1, 0.6$

k	0.1	0.6	Variation
Amplitude (B)	5.026e-4	2.094e-3	416.6%
Phase (β)	18°	0°	-18°
Avg ($C_{m,avg}$)	-0.04270	-0.04560	106.8%

The negative values of C_m show a negative pitching moment (nose-down moment) around the first quarter of the chord. This negative values tend to reduce the angle of attack the wing is feeling. The minimum values of both cases can be related to the maximum values of C_L seen in Figure 5.6. Maximum lift is produced when the tip is moving downwards, creating a lift increment ΔC_L due to the local angle of attack. This local ΔC_L is generated behind the moment axis, which creates a lever arm that produces this increment in the nose-down moment.

The difference in amplitude between the two cases can be related to the difference in amplitude in the lift coefficient and the relative angle of attack the tip experiences. A shift in the phase is also related to the phase of the C_L. A maximum in lift experienced later provides a lever arm acting later. A difference of 7% in he $C_{m,avg}$ for the same angle of attack cannot be easily understood for the same wing. The pressure coefficient for both cases at the MAC is compared in Figure 5.11.

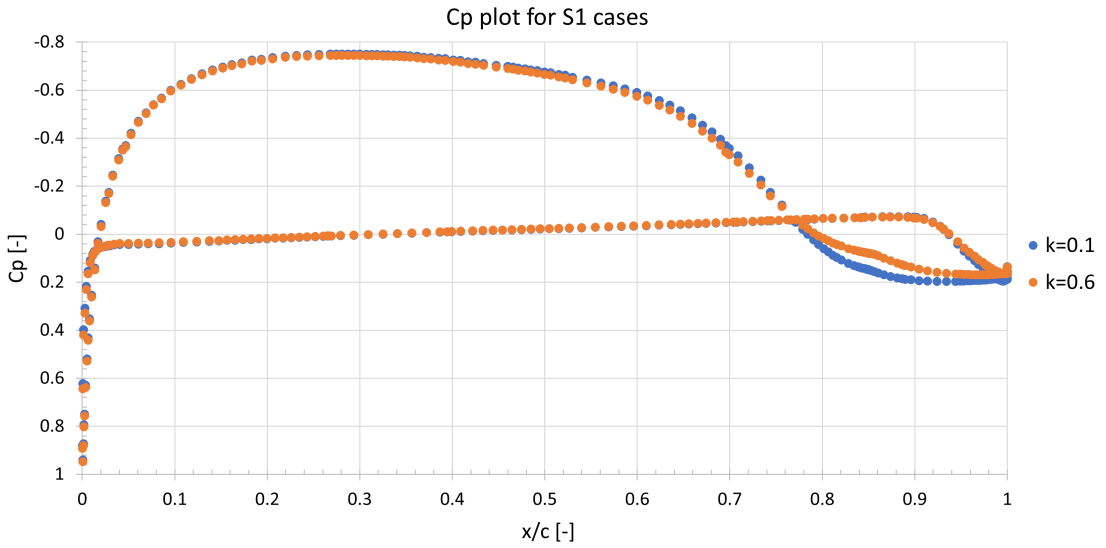

Figure 5.11: C_p plot for the cases in S1 at the MAC

From the plot it can be stated that the pressure distribution for both cases is almost identical, except at the upper surface of the aileron. A higher pressure is produced in this section of the wall for $k = 0.1$. This increase in pressure pushes down the back of the wing, which is translated in a nose up moment in comparison to $k = 0.6$. The velocity contours for the same section of the wing at the aileron can be seen in Figure 5.12.

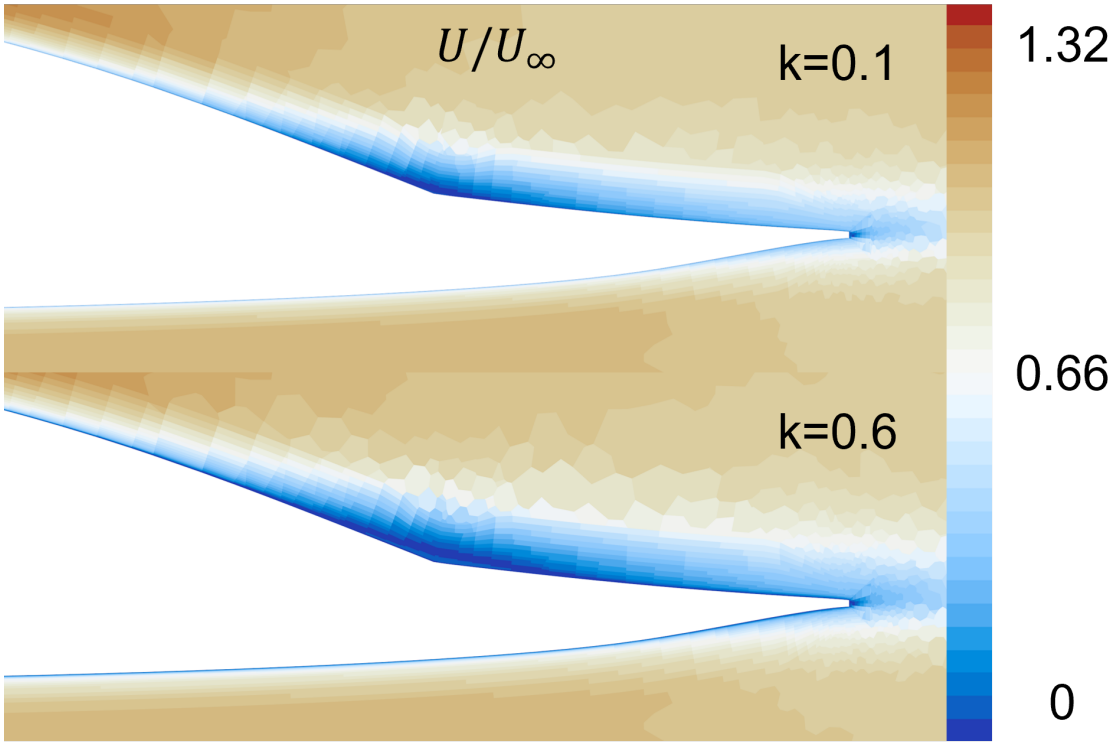

Figure 5.12: Relative velocity contours at the aileron for S1

The pressure increase at the aileron with $k = 0.1$ is given by the low velocity bubble that appears in the intersection of the aileron with the rest of the airfoil. This bubble remains attached to the wall, providing the pressure increment. With $k = 0.6$ the same bubble appears, but it is not completely attached, as higher relative velocities are seen between the bubble and the wall. A reason for this separation could be the design of the laminar airfoil. The conditions found for $k = 0.6$ are not the expected during flight due to the low velocity of 7.74 m/s. Such a difference in Re, from 3.3e5 to 2e6, can be cause of the difference in C_{mavg}. Another explanation to this can be the mesh not being appropriate to one of the cases. The mesh is designed to predict the behaviour of the fluid at $Re = 2e6$. The difference in order of magnitude of Re could be causing flaws in the solution for $k = 0.6$, as detachments of the boundary layer are not expected for low AoA.

5.1.4 Generalized Forces for S1, $k = 0.1$

The generalized forces acting over the wing for the deformation related to S1 are obtained. Only the forces in the Z component are taken into account in this study. This consideration is taken because only this component is obtained from the DLM study. The DLM provides this generalized forces in the Fourier domain, as a function of the reduced frequency.

For each reduced frequency and vibration mode, the procedure presented in this section should be followed. An increase in the number of modes analysed means an increase in the computational time and storage due to mapping. It has been decided that the components of twenty generalized forces are obtained. The generalized forces can be obtained from the total forces acting over the wing and the eigenvectors of the mode of the specific coordinate. This is previously explained in Section 4.5.4. The expression is shown in Equation 5.7.

$$f_{gen,rj} = \Phi_j^T \cdot F'_{Tr} \tag{5.7}$$

The forces obtained have a sinusoidal behaviour due to the nature of the vibration mode. The elements in the GAF provide a modification in amplitude and phase to the sinusoidal behaviour of the generalized force. The phase and amplitude of each of the generalized forces are obtained approximating to a function of the form $f_{gen,rj}(t) = B\sin(\omega_r t + \beta)$. They are seen in Table 5.4.

Table 5.4: Constants describing f_{gen} for S1, $k = 0.1$, 20 modes

Mode	Amplitude (B; m^3)	Phase (β; °)	Mode	Amplitude (B; m^3)	Phase (β; °)
1	3.797e-4	-73.79	11	2.853e-4	108.01
2	2.733e-5	-73.79	12	1.621e-5	-75.59
3	1.732e-5	-73.79	13	2.958e-4	-80.99
4	3.669e-3	104.41	14	3.878e-4	100.81
5	8.787e-4	106.21	15	3.585e-4	-80.99
6	6.138e-3	106.21	16	4.106e-5	95.41
7	4.333e-3	106.21	17	4.002e-6	-80.99
8	1.880e-3	106.21	18	1.056e-6	261.01
9	1.391e-3	106.21	19	4.447e-5	-82.79
10	9.560e-5	102.61	20	1.461e-4	-79.19

The amplitude and phase of the generalized function can be seen as a complex quantity (Z_{rj}) multiplying the ordinal sinusoidal function as $f_{gen,rj}(t) = Z_{rj} \sin(\omega_r t)$. Each element of the generalized forces vector can be seen as a linear function of the displacement of one mode ($q_r(t)$). It is defined in modal coordinates in Equation 5.8

$$q_r(t) = \frac{A}{|\Phi_r|_{max}} \sin(\omega_r t) \tag{5.8}$$

The linear relation of the displacement with the generalized forces is then presented in Equation 5.9.

$$f_{gen,rj}(t) = \frac{Z_{rj} \cdot |\Phi_r|_{max}}{A} \cdot q_r(t) \tag{5.9}$$

If this equation is translated to the frequency domain and compared to Equation 5.10

$$f_{gen,rj} = q_\infty GAF_{rj}(k) \cdot q_{r,0} \tag{5.10}$$

Similarly to the methodology followed by Verdonck et al. (2019), the description of the GAF as known elements coming from CFD is seen in Equation 5.11.

$$GAF_{rj}(k) = \frac{Z_{rj}(k) \cdot |\Phi_r|_{max}}{A \cdot q_\infty} \tag{5.11}$$

Where each element GAF_{rj} is a function of the generalized forces through Z_{rj} and is normalized to the values of the amplitude of the displacement, the dynamic pressure and the maximum displacement of the mode shape. After the calculations are performed, the GAF elements for S1 $k = 0.1$ are obtained for the first twenty modes. The results are shown in Table 5.5.

The elements obtained conform a vector contained in the GAF matrix. This vector relates the effects of the forces generated by the vibration mode S1 with each of the other vibration modes. The matrix depends on the reduced frequency. In this case $k = 0.1$. The elements of the vector can be compared to the results obtained with the DLM.

Table 5.5: GAF elements for S1, $k = 0.1$, 20 modes

Mode	Re($GAF_{S1,j}$)	Im($GAF_{S1,j}$)	Mode	Re($GAF_{S1,j}$)	Im($GAF_{S1,j}$)
1	1.654e-5	-5.688e-5	11	-1.376e-5	4.232e-5
2	1.190e-6	-4.094e-6	12	6.291e-7	-2.448e-6
3	7.543e-7	-2.594e-6	13	7.227e-6	-4.557e-5
4	-1.425e-4	5.543e-4	14	-1.135e-5	5.942e-5
5	-3.827e-5	1.316e-4	15	8.759e-6	-5.523e-5
6	-2.673e-4	9.194e-4	16	-6.040e-7	6.376e-6
7	-1.887e-4	6.490e-4	17	9.777e-8	-6.165e-7
8	-8.186e-5	2.815e-4	18	-2.573e-8	-1.627e-7
9	-6.058e-5	2.084e-4	19	8.707e-7	-6.882e-6
10	-3.256e-6	1.455e-5	20	4.275e-6	-2.239e-5

5.2 Mode SR2

The shape induced in the wing by SR2 is intended to be described as a combination of bending and torsion modes. The understanding of the behaviour of this vibration mode can be assessed through the eigenvectors belonging to the mode. These eigenvectors are shown in Figure 5.13.

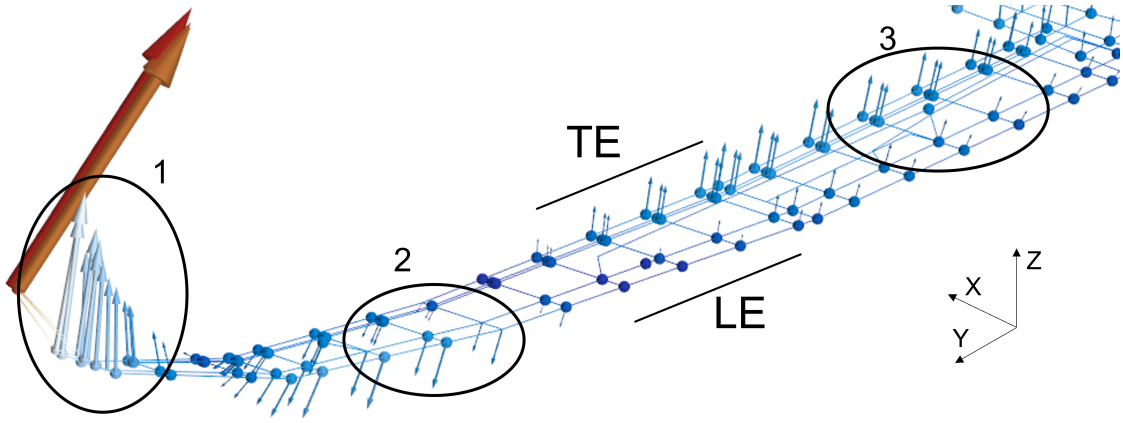

Figure 5.13: Different behaviour of the eigenvectors across the wing for SR2

The eigenvectors conform different shapes across the wing in each spanwise section. Three different zones are identified. In zone 1 in Figure 5.13 the eigenvectors have approximately the same direction (upwards) and magnitude. In zone 2 the eigenvectors that are closer to the LE have a higher magnitude than the ones closer to the TE, but all have a downwards

direction. In zone 3 the opposite case appears, higher magnitudes of the eigenvectors are located close to the trailing edge, while the LE remains with lower values, but they have an upwards direction. The variation of the behaviour of the mode across the span, does not allow the assumption of this mode as a 2D shape. Therefore, a theoretical approach to the lift oscillation cannot be performed.

5.2.1 Variations of C_L with k for SR2

The evolution of the C_L is studied for the different reduced frequencies of SR2. The plot of the C_L against the time is seen in Figure 5.14.

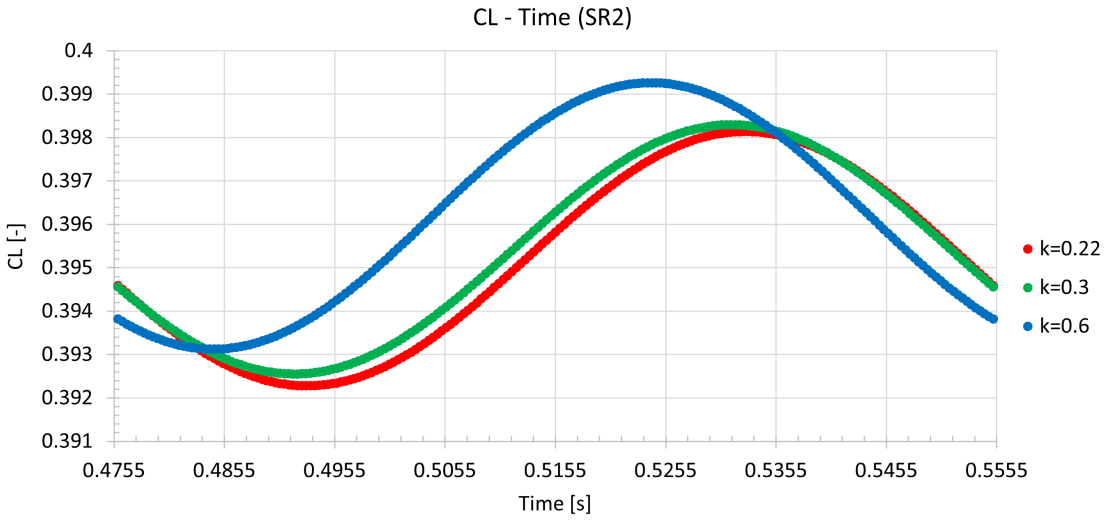

Figure 5.14: Evolution of the C_L for the mode SR2 as a function of time

The phase shift from lower to higher k can be understood from the delay produced by the variation of the free-stream velocity. The amplitude of the lift oscillations seem to not vary as much as for mode S1. For mode SR2, different torsional behaviours are the main motion observed. The relative angle of attack is mainly modified by the rotation of the wing. This rotation does not provide a vertical component to the mean velocity seen by the whole wing. An increment in the angle of attack is not perceived. The effect can be seen in Figure 5.15.

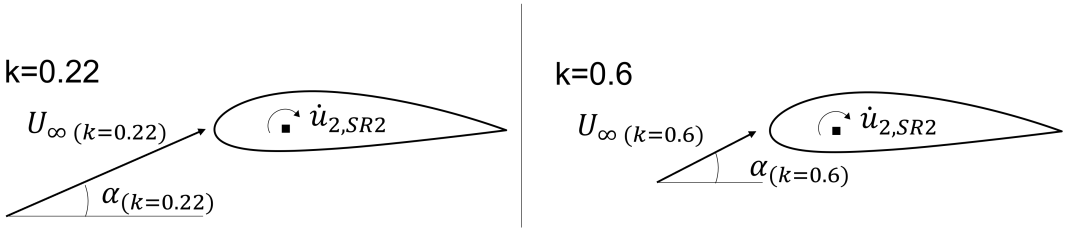

Figure 5.15: Different increments in AoA for the different values of k

However the average value of the lift coefficients observed is not the same for the different reduced frequencies. The pressure distribution over the MAC is studied from Figure 5.16.

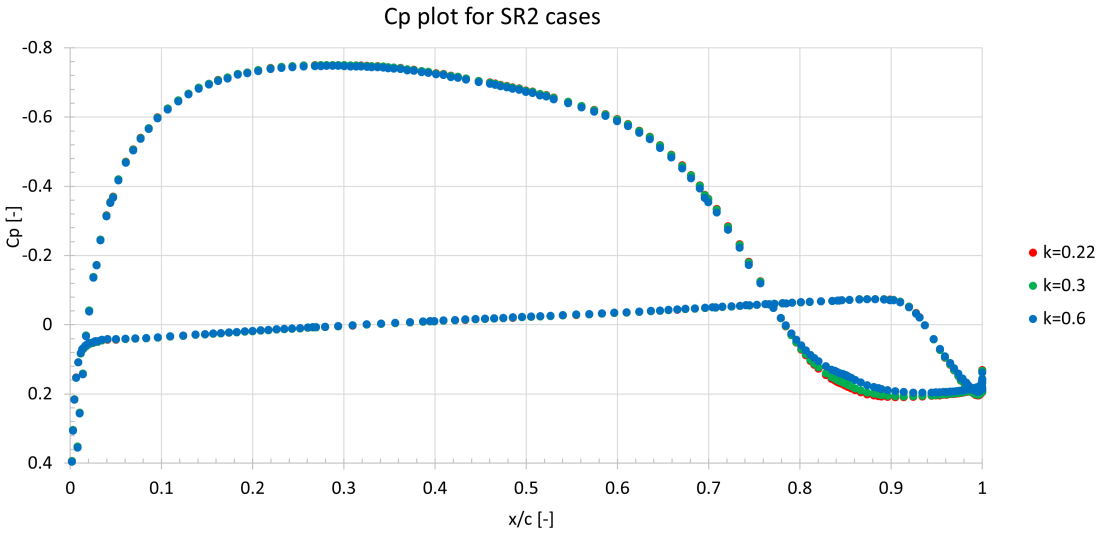

Figure 5.16: C_p plot for the cases in SR2 at the MAC

It is seen that there exist variations of the pressure distribution at the aileron of the MAC. However this section of the wing lies in between zones 2 and 3 from Figure 5.13 and is not representative on the behaviour of the wing. The plot of one section does not allow a complete description of the lift variations. The pressure coefficient is now plotted spanwise. In Figure5.17 the wing of the aircraft is represented with a red line where the C_p is obtained. Only $k = 0.22$ and $k = 0.6$ are represented because they represent the greatest variation.

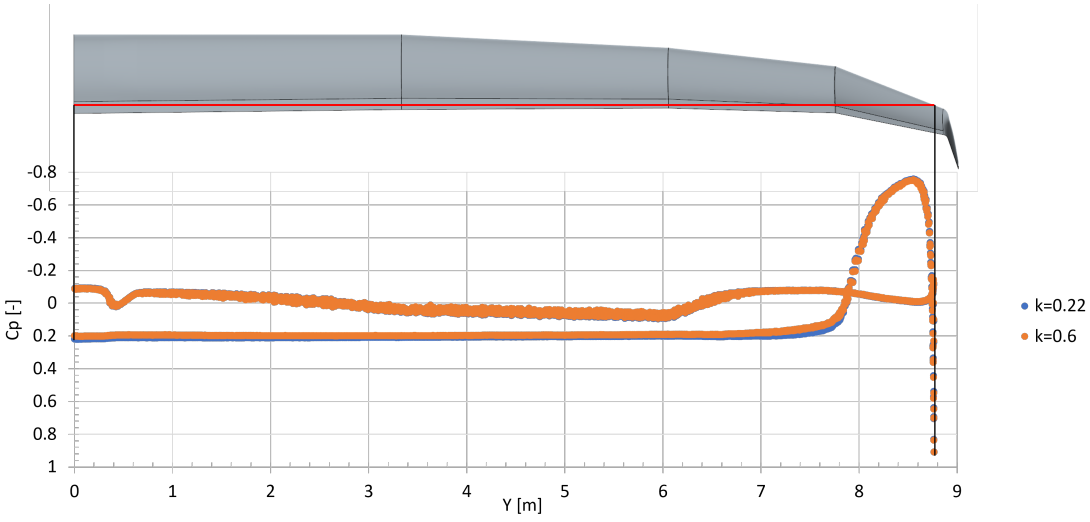

Figure 5.17: Pressure distribution along the ailerons

The area of the ailerons is chosen. The variations in the pressure distributions have been observed mainly in these areas. Figure 5.17 shows higher values of pressure for the upper part of the aileron at $k = 0.22$. Higher pressure at the suction side can be considered a loss of lift with respect to the other case.

The two plots of the C_p show an expected C_L higher for the $k = 0.6$. But no other explanation than the Re seems to account for the variations in the mean lift. This variation in lift is very small compared to the lift itself, and can be assumed to be a variation due to the high differences in Re. Table 5.6 compares both values of the average lift and Re in the oscillations.

Table 5.6: Comparison of average lift for SR2

k	C_{Lavg}	Re	Variation
0.6	0.39620	1.80e-6	base
0.22	0.39521	4.30e-6	-0.25%

Time convergence of the results can be verified through the plot of the C_L against the oscillation over the wing. The cases of SR2 are seen in Figure 5.18.

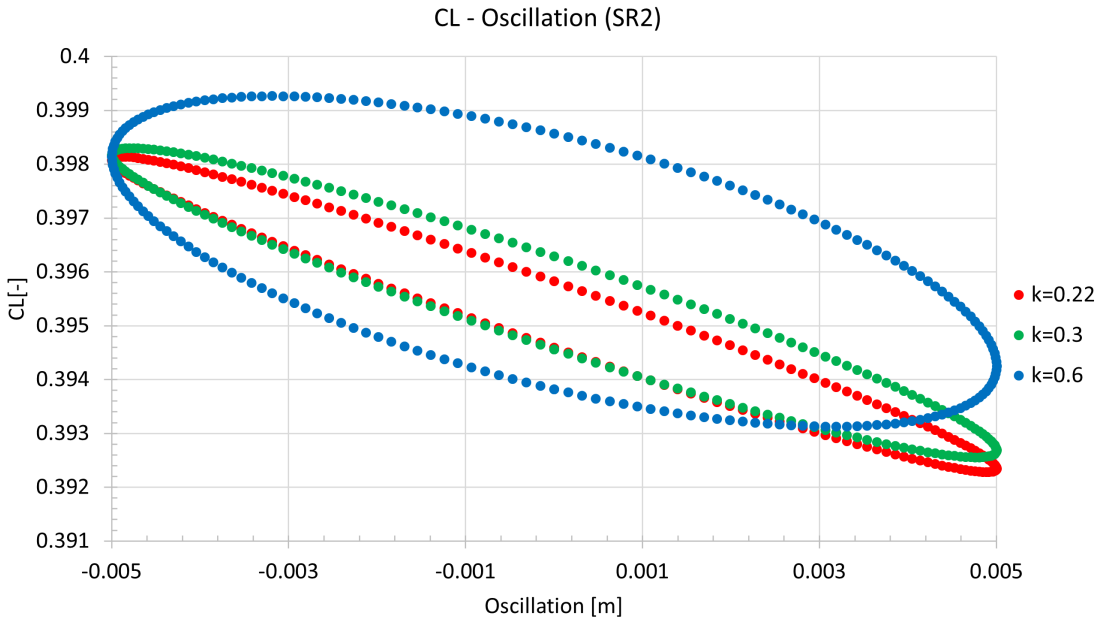

Figure 5.18: Evolution of the C_L for the mode SR2 as a function of the oscillation

In this type of plot the phase of the oscillation can be seen in the semi-minor axis of the ellipse. The lower the reduced frequency, the thinner is the ellipse, meaning that for the quasi-steady

case a linear variation would be observed. Differently to the case of S1, this line would create a variation in lift. The torsion created by SR2 would generate a difference in angles of attack in the quasi-steady case.

5.2.2 Variations of C_m with k for SR2

After analysing the small differences in the pressure distributions of Section 5.2.1, the C_m variations over time shown in Figure 5.19 can be studied.

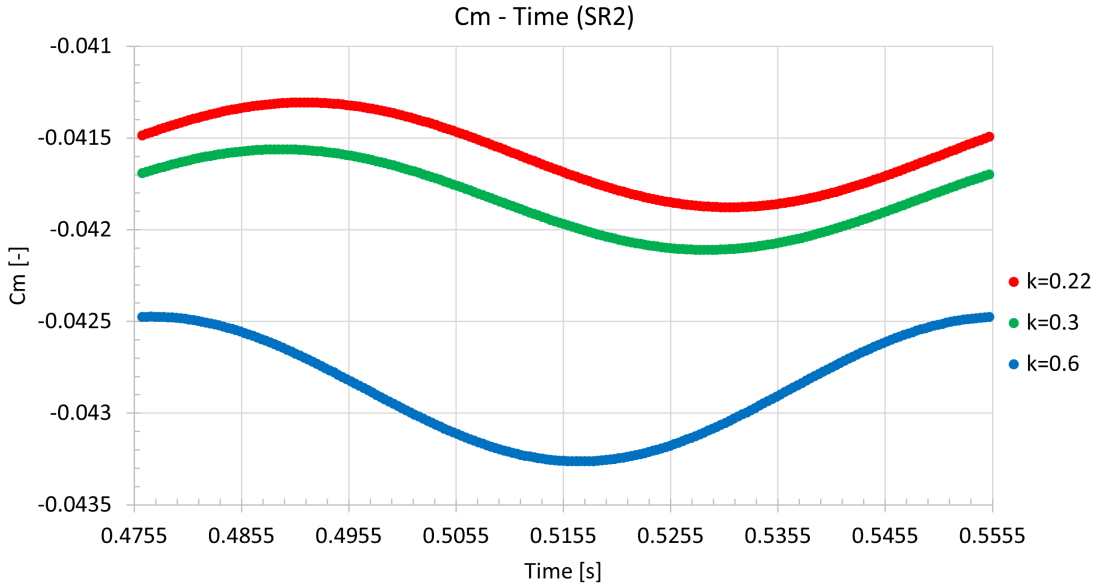

Figure 5.19: Evolution of the C_m for the mode SR2 as a function of time

The higher pressures observed at the upper surface of the aileron produce a increment in the force pushing downwards for lower reduced frequencies. This behaviour is the same as the one described for the vibration mode S1. This increment in forces downwards creates a pitching moment with nose-up direction.

6 Summary and Outlook

In this thesis, the unsteady aerodynamics of a high-aspect ratio wing have been examined and described in detail. Two vibration modes have been studied. These may occur at the flutter boundary and have been applied to the geometry of the wing in CFD. For each of the vibration motions, a description of the unsteady phenomena has been proposed aided by the aerodynamic coefficients C_L, C_m and C_p. This analysis extends to comparing different reduced frequencies for both vibration modes.

In order to perform the unsteady simulations, a pre-processing stage needs to be performed. A methodology for the preparation of the simulation has been developed for the project. In this methodology the different steps needed to couple FEM and CFD have been explained. This methodology can be followed to study other vibration modes than the ones included in this thesis.

A considerable amount of simulation files have been obtained through this work as an output from the methodology followed. These simulation files will serve as a starting point for future analysis in the unsteady behaviour of the wing. The process chain that is being created intends to study more reduced frequencies and vibration modes. The simulation files produced will reduce the time required to generate the setup for the simulations. This reduction in time is proven useful in order to compare CFD results to the ones obtained with the DLM, as time is the main limitation in the usage of CFD.

One of the purposes of CFD in the scope of the ProFla project is the correction of the GAF matrix obtained with the DLM. The obtention of the elements in this matrix has been explained. Furthermore, the results have been obtained for a reduced frequency of one of the vibration modes. The exact same procedure that has been explained can be followed for other setups.

A theoretical approach to the problem solution has also been performed. Starting from the 2D flutter theory described by Theodorsen (1949), the 3D wing has been approximated to the 2D case. It has been proven that this approach is not feasible in the flutter analysis of a complex wing. For the simple bending studied, the results are not comparable. For any vibration mode that is not a simple bending or torsion, the assumption of 2D is not even possible.

The main limitation of this work is the use of a single mesh for every case studied. One of the main purposes of CFD in flutter analysis is to account for the error that arises from assuming an inviscid flow in the DLM. By not changing the mesh for different Re the viscosity effects

at the boundary layer are not well described. A tool like Ansys ICEM, that generates a mesh more efficiently than STAR-CCM+ could be helpful implemented in the process chain for future simulations.

Overall, the main objectives proposed for the thesis have been fulfilled, emphasising the obtention of the GAF coefficients and the creation of a methodology for future research. During the process, time and task management have been the most important aspects to take into account, as the limitations due to long computational times are considerable. The improvement in usage of macros for the STAR-CCM+ simulations has been key to finishing before the deadline. The procedure followed the first months of the project would have led to longer and more repetitive processes of pre-processing and post-processing. This can be acknowledged from the prolongation of one month to the initial deadline.

Bibliography

Albano, E. and Rodden, W. P. (1969). A Doublet-Lattice Method for Calculating Lift Distributions on Oscillating Surfaces in Subsonic Flows. *AIAA Journal*, 7(2).

Anderson, J. D. (2017). *Fundamentals of Aerodynamics*. McGraw-Hill series in Aeronautical and Aerospace Engineering. McGraw-Hill.

Bisplinghoff, R. L., Ashley, H., and Halfman, R. L. (1996). *Aeroelasticity*. Dover Publications.

Blair, M. (1992). A Compilation of the Mathematics Leading to the Doublet Lattice Method. Technical Report ADA256304, WRIGHT LAB WRIGHT-PATTERSON AFB OH.

Blazek, J. (2015). *Computational Fluid Dynamics: Principles and Applications*. Elsevier.

Brunton, S. L. and Rowley, C. W. (2009). Modeling the Unsteady Aerodynamic Forces on Small-Scale Wings. *AIAA Paper 2009-1127*.

Collar, A. R. (1978). The First Fifty Years of Aeroelasticity. *Aerospace, 5, 2, 12-20*.

Ferzinger, J. H. and Peric, M. (2002). *Computational Methods for Fluid Dynamics*. Springer.

Förster, M. (2016). *Aeroelastische Stabilitäts- und Antwortanalyse auf Basis Numerischer Strömungssimulation*. PhD thesis, TU München.

Giesing, J. P., Kalman, T. P., and Rodden, W. P. (1976). Correction Factor Techniques for Improving Aerodynamic Prediction Methods. Technical Report NASA CR-144967, NASA.

Luke, Y. L. and Dengler, M. A. (1951). Tables of the Theodorsen Circulation Function for Generalized Motion. *Journal of the Aeronautical Sciences*.

Mendl, D. (2022). Modelloptimierung eines Strukturdynamischen Modells eines Hochleistungs-Segelflugzeuges anhand eines Standschwingungsversuches. Bachelor's thesis, TU München.

Palacios, R., Climent, H., Karlsson, A., and Winzell, B. (2001). Assessment of Strategies for Correcting Linear Unsteady Aerodynamics Using CFD or Test Results. *IFASD2001-074*.

Perry, B. (2017). Comparison of Theodorsen's Unsteady Aerodynamic Forces with Doublet Lattice Generalized Aerodynamic Forces. *NASA/TM-2017-219667*.

Quinlan, J. R. and Gern, F. H. (2018). Update on the Development of a Flutter Analysis Capability for Unconventional Aircraft Concepts using HCDstruct. *AIAA 2018-4146*.

Rambla Areal, V. (2022). CFD Analysis of the Laminar-Turbulent Transition on a Sailplane Wing. Bachelor's thesis, TU München.

Reynolds, O. (1895). On the Dynamical Theory of Incompressible Viscous Fluids and the Determination of the Criterion. *Philosophical Transactions of the Royal Society of London*, 186(126-164).

Rozov, V., Hermanutz, A., Breitsamter, C., and Hornung, M. (2017). Aeroelastic Analysis of a Flutter Demonstrator With a Very Flexible High-Aspect-Ratio Swept Wing. *IFASD-2017-173*.

Siemens (2021). *Simcenter STAR-CCM+ Documentation Version 2021.3*. Siemens Digital Industries Software.

Thelen, A., Leiffson, L., and Beran, P. (2020). Multifidelity Flutter Prediction Using Local Corrections to the Generalized AIC. *Aerospace Science and Technology*, 106(106032).

Theodorsen, T. (1949). General Theory of Aerodynamic Instability and the Mechanism of Flutter. Technical Report NACA-TR-496.

Verdonck, H., Thormann, R., Bleecke, H., and Stickan, B. (2019). Error Estimation and POD-Based Reference Selection to Approximate GAF Matrices for Flutter. *IFASD-2019-25*.

Versteeg, H. K. and Malalasekera, W. (2007). *An Introduction to Computational Fluid Dynamics: The Finite Volume Method*. Pearson.

Wright, J. R. and Cooper, J. E. (2007). *Introduction to Aircraft Aeroelasticity and Loads*. John Wiley and Sons.

Yao, W. and Marques, S. (2017). Application of a High-Order CFD Harmonic Balance Method to Nonlinear Aeroelasticity. *Journal of Fluids and Structures*.

Declaration of Authorship

I hereby declare that the thesis submitted is my own unaided work. All direct or indirect sources used are acknowledged as references.

I am aware that the thesis in digital form can be examined for the use of unauthorized aid and in order to determine whether the thesis as a whole or parts incorporated in it may be deemed as plagiarism. For the comparison of my work with existing sources I agree that it shall be entered in a database where it shall also remain after examination, to enable comparison with future theses submitted. Further rights of reproduction and usage, however, are not granted here.

This paper was not previously presented to another examination board and has not been published.

Garching, 1st. July 2023

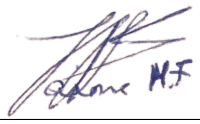

Jaime Martín Ferres

A Appendix: C_D Plots

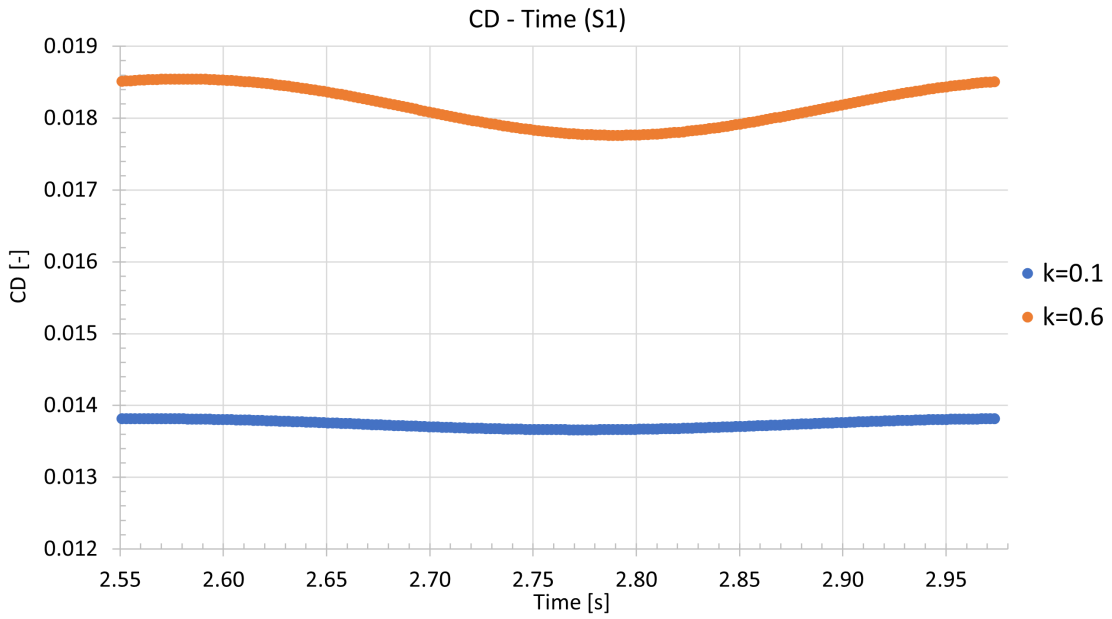

Figure A.1: Evolution of the C_D for the mode S1 as a function of time

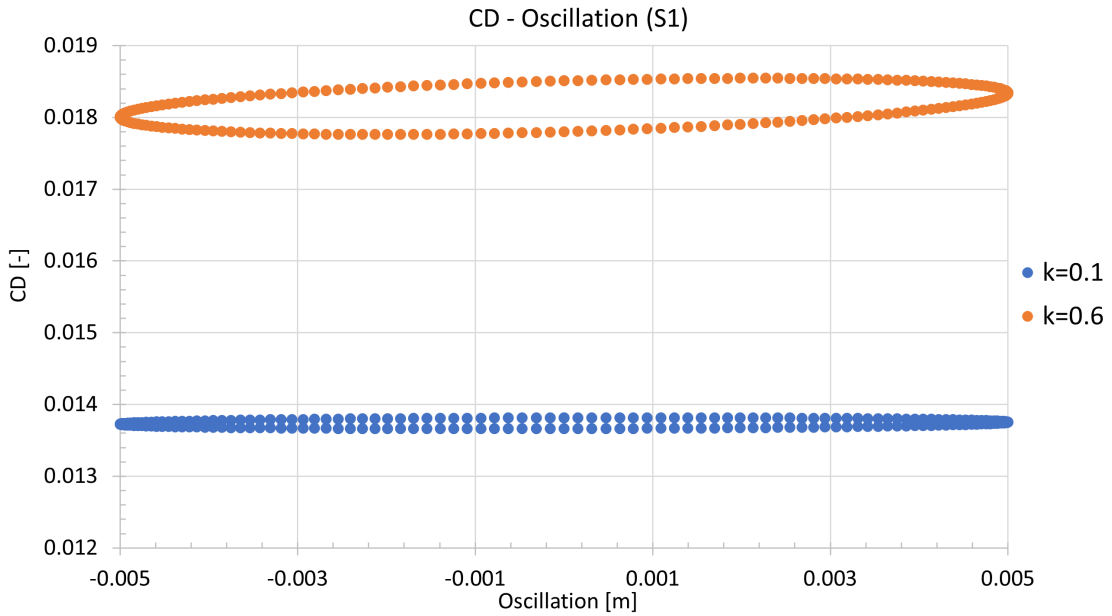

Figure A.2: Evolution of the C_D for the mode S1 as a function of the oscillation

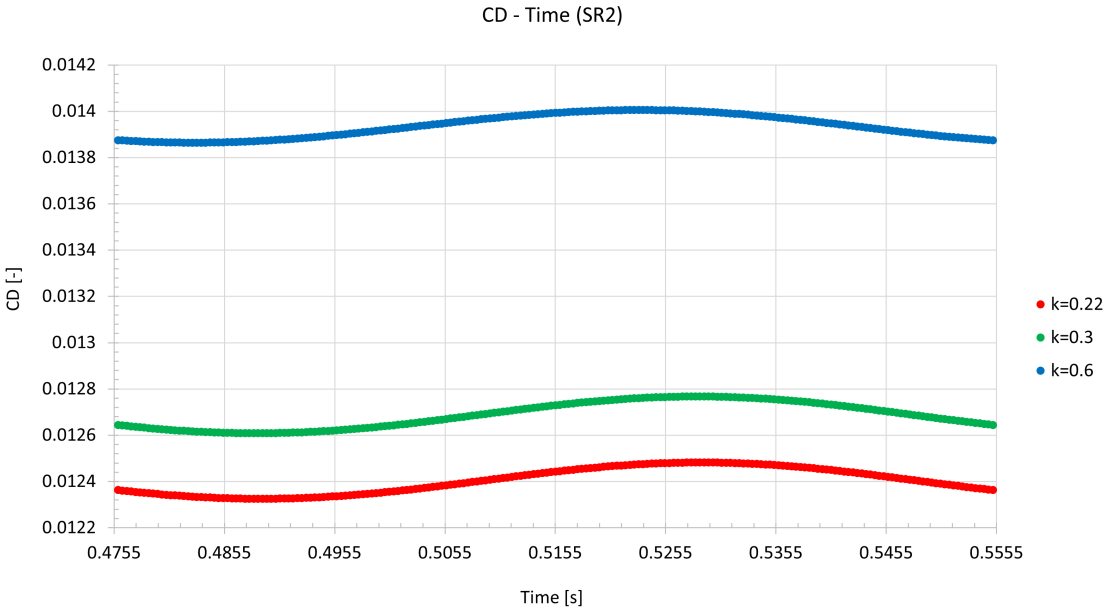

Figure A.3: Evolution of the C_D for the mode SR2 as a function of time

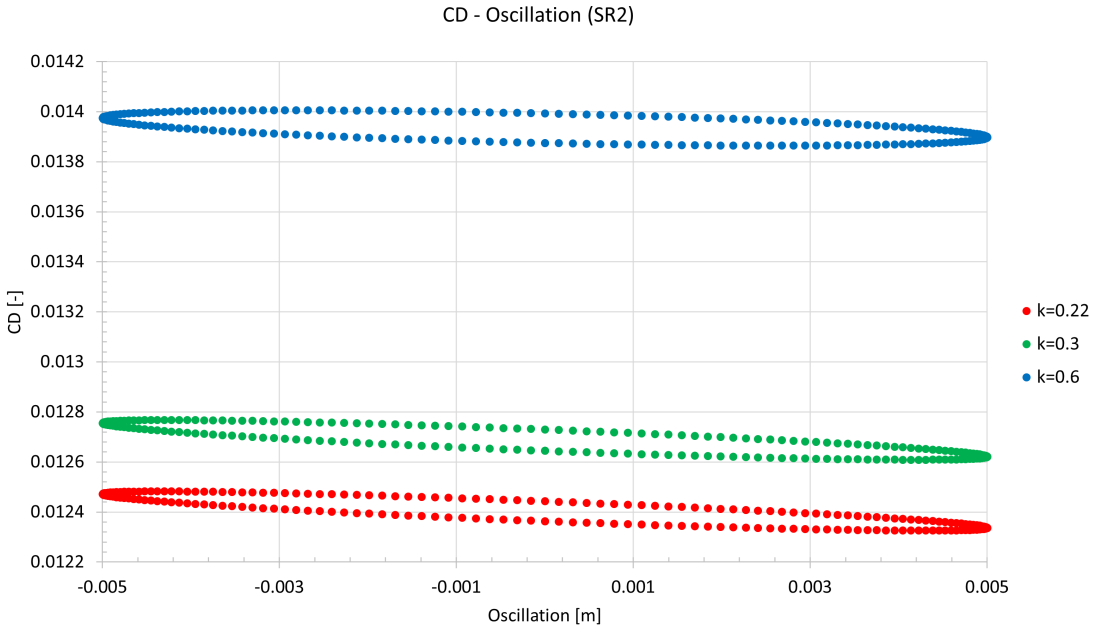

Figure A.4: Evolution of the C_D for the mode SR2 as a function of the oscillation

B Appendix: Examples of Macros for STAR CCM+ in Java

Parameter Definition Example

```
package macro;

import java.util.*;

import star.common.*;
import star.base.neo.*;

public class parameter_definition extends StarMacro {

  public void execute() {
    execute0();
  }

  private void execute0() {

    Simulation simulation_0 =
      getActiveSimulation();

    ScalarGlobalParameter scalarGlobalParameter_0 =
      ((ScalarGlobalParameter)
      simulation_0.get(GlobalParameterManager.class).
      getObject("Total Sim Time"));

    scalarGlobalParameter_0.getQuantity().
    setDefinition("${Period_duration}");

    ImplicitUnsteadySolver implicitUnsteadySolver_0 =
      ((ImplicitUnsteadySolver) simulation_0.getSolverManager().
      getSolver(ImplicitUnsteadySolver.class));

    implicitUnsteadySolver_0.getTimeStep().
    setDefinition("${Time}<4*${Period_duration}?${timestep_1}:
    ((${Time}>=3*${Period_duration})?${timestep_2}:0)");

  }
}
```

Generalized Forces Export

```
package macro;

import java.util.*;

import star.common.*;
import star.base.neo.*;

public class export_f_gen extends StarMacro {

  public void execute() {
    execute0();
  }

  private void execute0() {

    Simulation simulation_0 =
      getActiveSimulation();

for (int i = 1; i <= 29; i++) {

    String plotName = "F_gen_" + i;

    MonitorPlot monitorPlot = (MonitorPlot) simulation_0.getPlotManager().
    getPlot(plotName);

    String filePath = resolvePath("P:PATH\\f_gen_" + i + "_k_0.22.csv");

    monitorPlot.export(filePath, "\t");
}
  }
}
```

Scene Export

```
package macro;

import java.util.*;

import star.common.*;
import star.base.neo.*;
import star.vis.*;

public class pressure_scene extends StarMacro {

  public void execute() {
    execute0();
  }

  private void execute0() {

    Simulation simulation_0 =
      getActiveSimulation();

    Scene scene_0 =
      simulation_0.getSceneManager().getScene("Pressure_coeff");

    scene_0.initializeAndWait();

    scene_0.open();

    SceneUpdate sceneUpdate_0 =
      scene_0.getSceneUpdate();

   ScalarDisplayer scalarDisplayer_0 =
      ((ScalarDisplayer) scene_0.getDisplayerManager().
      getObject("Scalar 1"));

    scalarDisplayer_0.getScalarDisplayQuantity().
    setAutoRange(AutoRangeMode.NONE);

    scene_0.getAnnotationPropManager().getAnnotationGroup().
    setQuery(null);

    TimeStepUpdateFrequency timeStepUpdateFrequency_0 =
      sceneUpdate_0.getTimeStepUpdateFrequency();

    timeStepUpdateFrequency_0.setTimeSteps(3);

    hardcopyProperties_0.setOutputMagnification(4);
  }
}
```

Steady to Unsteady Simulation

```
package macro;

import java.util.*;

import star.common.*;
import star.base.neo.*;
import star.morpher.*;

public class steady_to_unsteady extends StarMacro {

  public void execute() {
    execute0();
  }

  private void execute0() {

    Simulation simulation_0 =
      getActiveSimulation();

    PhysicsContinuum physicsContinuum_0 =
      ((PhysicsContinuum) simulation_0.getContinuumManager().
      getContinuum("Physics"));

    SteadyModel steadyModel_0 =
      physicsContinuum_0.getModelManager().
      getModel(SteadyModel.class);

    physicsContinuum_0.disableModel(steadyModel_0);

    physicsContinuum_0.enable(ImplicitUnsteadyModel.class);

    Units units_0 =
      simulation_0.getUnitsManager().
      getInternalUnits(new IntVector(new int[]
      {0,0,1,0,0,0,0,0,0,0,0,0,0,0,0,0,0,0,0,0,0,0,0,0}));

    ImplicitUnsteadySolver implicitUnsteadySolver_0 =
      ((ImplicitUnsteadySolver) simulation_0.getSolverManager().
      getSolver(ImplicitUnsteadySolver.class));

    implicitUnsteadySolver_0.getTimeStep().
    setDefinition("${Time}<3*${Period_duration}?${timestep_1}:
␣␣␣␣((${Time}>=3*${Period_duration})?${timestep_2}:0)");

    implicitUnsteadySolver_0.getTimeDiscretizationOption().
    setSelected(TimeDiscretizationOption.Type.SECOND_ORDER);
```

```
    MorpherSolver morpherSolver_0 =
      ((MorpherSolver) simulation_0.getSolverManager().
      getSolver(MorpherSolver.class));

    BSplineMorpherMethodSettings bSplineMorpherMethodSettings_0 =
      morpherSolver_0.getMorpherMethodSettingsManager().
      get(BSplineMorpherMethodSettings.class);

    Units units_1 =
      ((Units) simulation_0.getUnitsManager().getObject(""));

    bSplineMorpherMethodSettings_0.getTolerance().
    setValueAndUnits(1.0E-10, units_1);

    morpherSolver_0.setMorphFromZero(true);

    morpherSolver_0.setUseBoundaryLayerMorpher(true);
  }
}
```

C Appendix: Mode S1, $k = 0.3$ Plots

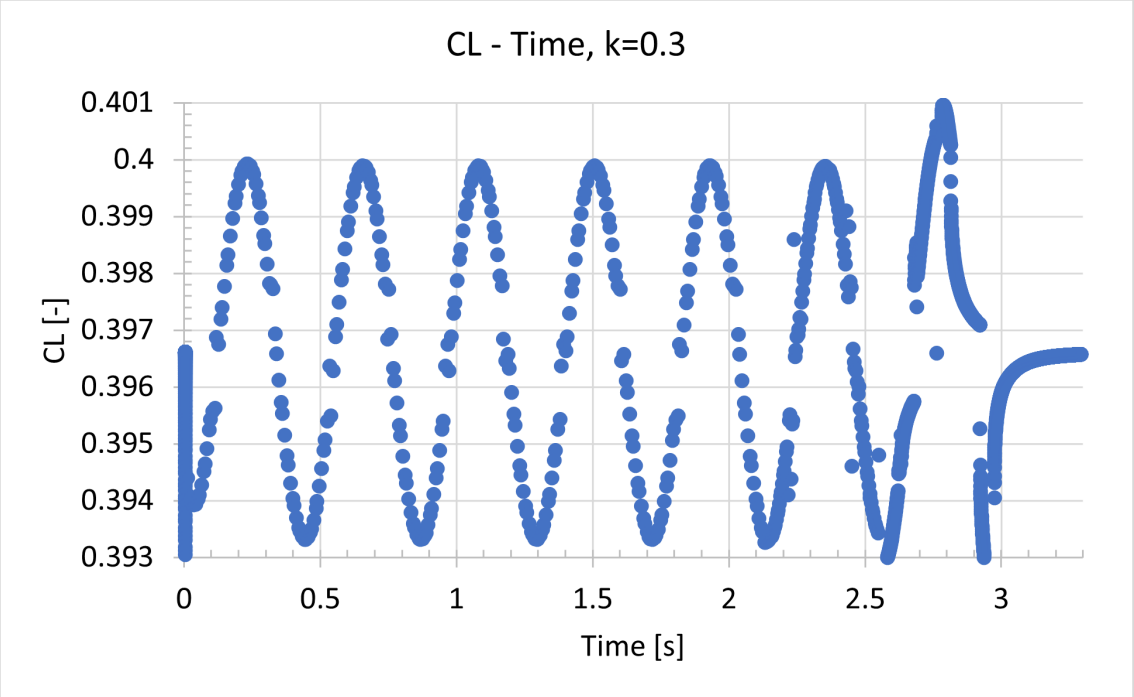

Figure C.1: Evolution of the C_L for the mode S1 $k = 0.3$ as a function of time

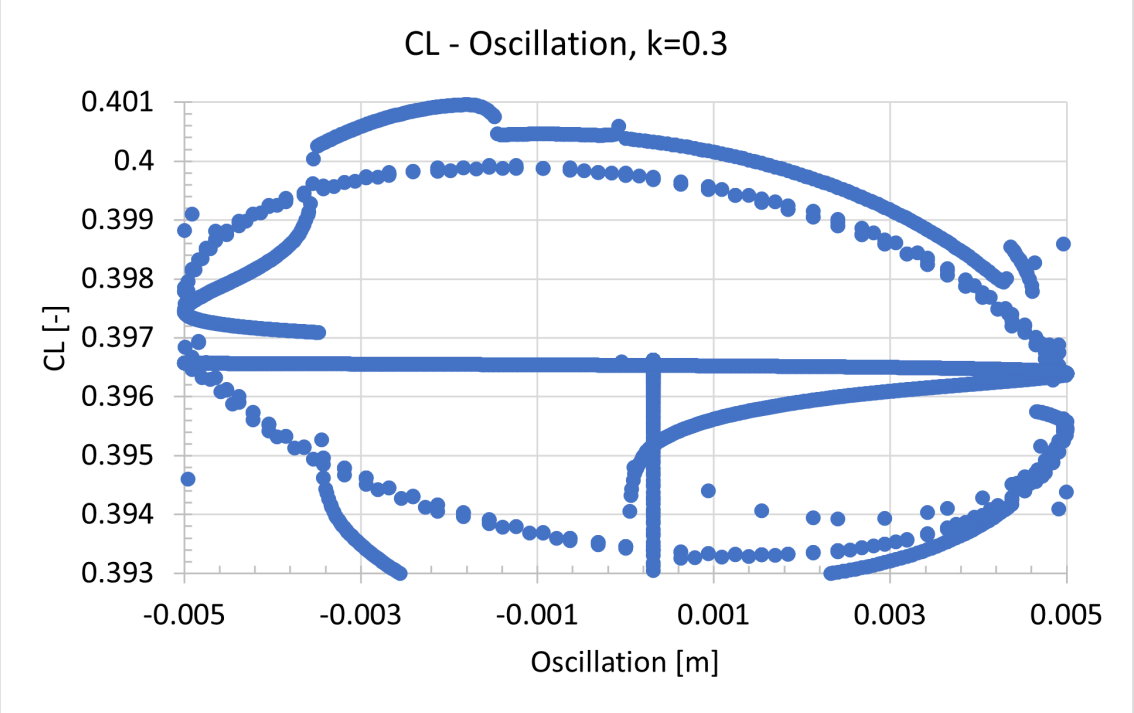

Figure C.2: Evolution of the C_L for the mode S1 $k = 0.3$ as a function of the oscillation

D Appendix: C_L Expression Computation

```
(*Define constants*)

clalpha = 0.091*180/Pi;   (*Define C_{Lalpha}*)
A = 0.005;                (*Define Amplitude*)
\[Omega] = 2.35*2*Pi;     (*Define frequency in rad/s*)
\[Phi]rat = 0.1484/1.03;  (*Define Eigenvalue ratio*)
c = 0.635;                (*Define c_{MAC}*)
clavg = 0.3963;           (*Define C_{Lavg}*)
Uinf01 = 46.46;           (*Define U_{\infty}*)
Ctheo01 = AbsArg[0.83192 + I*0.17230];
                          (*Define Theodorsen function for k=0.1*)

(*Define functions*)

u[t_] = -A*Sin[\[Omega]*t]*\[Phi]rat;
                          (*Define displacement*)
udot[t_] = -Ctheo01[[1]]*A*\[Omega]*\[Phi]rat*
   Cos[\[Omega]*t + Ctheo01[[2]]];
                          (*Define velocity including Theodorsen*)
CL01[t_] =
   clavg + clalpha*(c*D[D[u[t],t],t]/(4*Uinf01^2) + udot[t]/Uinf01);
                          (*Define lift function*)
```